Mathematical Medicine and Biology (2016) **33**, 123–157
doi:10.1093/imammb/dqv013
Advance Access publication on April 15, 2015

Computed tear film and osmolarity dynamics on an eye-shaped domain

LONGFEI LI[†], RICHARD J. BRAUN[*] AND TOBIN A. DRISCOLL
Department of Mathematical Sciences, University of Delaware, Newark, DE 19711, USA
[*]Corresponding author. Email: rjbraun@udel.edu

WILLIAM D. HENSHAW
Department of Mathematical Sciences, Rensselaer Polytechnic Institute, Troy, NY 12180, USA

JEFFREY W. BANKS[†]
Lawrence Livermore National Laboratory, Box 808, L-422, Livermore, CA 94551-0808, USA

AND

P. EWEN KING-SMITH
College of Optometry, The Ohio State University, Columbus, OH 43218, USA

[Received on May 26, 2014; revised on December 23, 2014; accepted on March 12, 2015]

The concentration of ions, or osmolarity, in the tear film is a key variable in understanding dry eye symptoms and disease. In this manuscript, we derive a mathematical model that couples osmolarity (treated as a single solute) and fluid dynamics within the tear film on a 2D eye-shaped domain. The model includes the physical effects of evaporation, surface tension, viscosity, ocular surface wettability, osmolarity, osmosis and tear fluid supply and drainage. The governing system of coupled non-linear partial differential equations is solved using the Overture computational framework, together with a hybrid time-stepping scheme, using a variable step backward differentiation formula and a Runge–Kutta–Chebyshev method that were added to the framework. The results of our numerical simulations provide new insight into the osmolarity distribution over the ocular surface during the interblink.

Keywords: lubrication theory; osmolarity dynamics; tear film; thin film; composite overlapping grid.

1. Introduction

The purpose of the model we develop here is to compute the dynamics of fluid motion and osmolarity of the tear film on an eye-shaped domain. Osmolarity is the concentration of ions in solution. Given an 1M concentration of NaCl solution, each molecule of salt dissociates into two ions, and the osmolarity is then 2 M. (Here M denotes molar concentration, which is moles per litre of solvent.) For a brief introduction to the mathematical models for the osmolarity and tear film dynamics, see the review by Braun (2012) or the paper by Zubkov *et al.* (2012).

The osmolarity is an important variable to include in tear film modelling because it is thought to be critical in the onset and subsequent development of dry eye syndrome (DES). A properly functioning tear film maintains a critical balance between tear secretion and loss within each blink cycle. Malfunction or deficiency of the tear film causes a collection of problems that are believed to comprise DES (Lemp, 2007). DES symptoms include, but are not limited to, blurred vision, burning, foreign body

[†]Present address: Department of Mathematical Sciences, Rensselaer Polytechnic Institute, Troy, NY 12180, USA.

sensation, tearing and inflammation of the ocular surface. Studies up to 2007 estimate that there are 4.91 million Americans suffering from DES (Anonymous, 2007). The ocular surface community is interested in understanding the function of the tear film (Johnson & Murphy, 2004) as well as the interaction of tear film dynamics and the connection between tear film volume, evaporation and break-up with DES (Anonymous, 2007).

We summarize a discussion of the role of osmolarity on the ocular surface from Baudouin *et al.* (2013) here. According to Tietz (1995), in healthy blood the osmolarity is in the range 285–295 Osm/m^3 (also expressed in mOsm/L or mOsM). In the healthy tear film, there is homoeostasis with the blood in the range 296–302 Osm/m^3 (Tomlinson *et al.*, 2006; Versura *et al.*, 2010; Lemp *et al.*, 2011). In DES, the lacrimal system is unable to maintain this homoeostasis and osmolarity values in the meniscus rise to 316–360 Osm/m^3 (Gilbard *et al.*, 1978; Tomlinson *et al.*, 2006; Sullivan *et al.*, 2010), and may rise to even higher values over the cornea. Using *in vivo* experiment and sensory feedback, Liu *et al.* (2009) estimated peak values of 800–900 Osm/m^3. Similar or higher values were computed from mathematical models of tear film break-up in King-Smith *et al.* (2010b) and Peng *et al.* (2014). We use a mathematical model to compute osmolarity over the entire exposed ocular surface subject to the assumptions stated in the Formulation section.

The method of tear sample collection and measurement is important. To our knowledge, osmolarity measurements in humans have been from samples in the inferior meniscus or the lower fornix. The lower fornix has a lower osmolarity than the meniscus (Mishima *et al.*, 1971), and samples from the meniscus are most commonly used today. Gilbard *et al.* (1978) summarized the use of prior measurement techniques that used pipettes or capillary tubes to collect tear samples. Older methods may have used pipettes that took too large a sample compared with the tear film total volume, and could induce reflex tearing. In the exquisitely sensitive eye, this is a significant concern that could dilute or otherwise change the chemistry of the tear sample. Some capillary techniques are difficult to use, and the method of Gilbard *et al.* (1978) appeared to be easier to use; we note that the paper does not indicate where in the inferior meniscus the measurement was taken. Subsequent to sample collection, older techniques relied on freezing point depression to determine the osmolarity of the sample to about 1% error. More recently, a calibrated resistance measurement using the TearLab device allows rapid determination of osmolarity with an error for in vitro samples of about 1–2% error (Lemp *et al.*, 2011; TearLab, 2013). In the approach, a sensor touches the meniscus at the temporal canthus, and the result is returned in less than a minute after the sample is taken. The latter approach is much more convenient for clinical use.

The level of effectiveness of osmolarity measurement to diagnose dry eye and to measure progression of the disease is still a matter of debate; for recent viewpoints, see for example Lemp *et al.* (2011), Amparo *et al.* (2013, 2014), Pepose *et al.* (2014) and Sullivan (2014). We found the summary by Baudouin *et al.* (2013) in their Sections 3 and 4 to be informative. We do not aim to settle the debate here, but to supply context for the measurements in the form of a quantitative prediction of the osmolarity over the entire exposed ocular surface to aid interpretation.

We now turn to previous work on the properties and dynamics of the tear film, relying heavily on the introduction from Li *et al.* (2014). Commonly, the tear film is described as a thin liquid film with multiple layers. At the anterior interface with air is an oily lipid layer that decreases the surface tension and retards evaporation, both of which help to retain a smooth well-functioning tear film (Norn, 1979). The aqueous layer is posterior to the lipid layer and consists mostly of water (Holly, 1973). At the ocular surface, there is a region with transmembrane mucins protruding from the cells in the corneal or conjunctival epithelia. This forest of glycosylated mucins, called the glycocalyx, has been referred to as the mucus layer in the past. It is generally agreed that the presence of the hydrophilic glycocalyx on the ocular surface prevents the tear film from dewetting (Bron *et al.*, 2004; Gipson, 2004;

Govindarajan & Gipson, 2010). The overall thickness of the tear film is a few microns (King-Smith *et al.*, 2004), while the average thickness of the lipid layer is on the order of 50–100 nm (Norn, 1979; King-Smith *et al.*, 2011) and the thickness of the glycocalyx is a few tenths of a micron (Govindarajan & Gipson, 2010). This structure is rapidly reformed, on the order of one second, after each blink in a properly functioning tear film.

The aqueous part of tear fluid is supplied from the lacrimal gland near the temporal canthus and the excess is drained through the puncta near the nasal canthus. Mishima *et al.* (1966) estimated the total tear volume and the rate of influx from the lacrimal gland, as well as the time for the entire volume of tear fluid to be replaced (tear turnover rate); Zhu & Chauhan (2005) reviewed experiments on tear drainage and developed a mathematical model for drainage rates of the aqueous component through the puncta. Doane (1981) proposed the mechanism of tear drainage *in vivo* whereby tear fluid is drained into the canaliculi through the puncta during the opening interblink phase. The drainage stops when the pressure equalizes in the canaliculi. Water lost from the tear film due to evaporation into air is an important process as well (Mishima & Maurice, 1961; Tomlinson *et al.*, 2009; Kimball *et al.*, 2010). This is the primary mechanism by which the osmolarity is increased in the tear film.

The supply and drainage of tear fluid affects the distribution and flow of the tear film. A number of methods have been used to visualize and/or measure tear film thickness and flow, including interferometry (Doane, 1989; King-Smith *et al.*, 2004; King-Smith *et al.*, 2009), optical coherence tomography (Wang *et al.*, 2003), fluorescence imaging (Harrison *et al.*, 2008; King-Smith *et al.*, 2013) and many others. We mention only a small number here that are relevant for our discussion of tear fluid flow over the exposed ocular surface. Maurice (1973) inserted lampblack into the tear film and watched the particle trajectories with a slit lamp. He observed that the particle paths in the upper meniscus near the temporal canthus diverge, with some particles proceeding towards the nasal canthus via the upper meniscus and others going around the outer canthus before proceeding towards the nasal canthus via the lower meniscus. (To our knowledge, no images from this experiment exist.) We use the term ‘hydraulic connectivity’ as shorthand for this splitting of flow connecting the menisci. A similar pattern of the tear film was observed by Harrison *et al.* (2008) using fluorescein to visualize the tear film thickness. In this experiment, concentrated sodium fluorescein is instilled in the eye. Shining blue light on the eye causes the fluorescein to glow green; the fluorescence allows one to visualize the tear film (Lakowicz, 2006). The concentration is such that if evaporation occurs, the concentration of fluorescein increases and the intensity of the fluorescence decreases; if fresh tear fluid enters the tear film, the concentration decreases and fluorescent intensity increases (Webber & Jones, 1986; Nichols *et al.*, 2012; Braun *et al.*, 2014). Harrison *et al.* (2008) visualized the entry of fresh tear fluid into the meniscus near the outer canthus, where the tear film was observed to brighten. Subsequently, this bright region split and fluid moved towards the nasal canthus along both the upper and lower lids via the menisci. The fluorescence could thus visualize hydraulic connectivity in the flow of tears. Similar experiments in King-Smith *et al.* (2013) and Li *et al.* (2014) visualized flow by using fluorescein instilled by drops in the tear film, and the mathematical model developed by Li *et al.* (2014) exhibited hydraulic connectivity in a very similar way to the experimental results shown in that paper.

The tear film is also redistributed near the eyelid margins by surface tension. The curvature generated by the meniscus creates a low pressure which draws in fluid from surrounding areas, creating locally thin regions near the meniscus. When fluorescein is used to visualize tear film thickness, this locally thin region near the lids is dark, and had been called the ‘black line’. The black line is typically thought to be a barrier between the meniscus at the lid margins and the rest of the tear film (McDonald & Brubaker, 1971; Miller *et al.*, 2002). Finally, though the healthy ocular surface is wettable, the tear film may still rupture; the term break-up is used in the ocular science community for this phenomenon. The surface

tension of the tear/air interface, the wettability of the ocular surface and the osmolarity are among the effects that we include in this study.

A variety of mathematical models have incorporated various important effects of tear film dynamics as recently reviewed by Braun (2012). The most common assumptions for these models are a Newtonian tear fluid and a flat cornea (Berger & Corrsin, 1974; Braun *et al.*, 2012). Tear film models are often formulated on a 1D domain oriented vertically through the centre of the cornea with stationary ends corresponding to the eyelid margins. We refer to models on this kind of domain as 1D models. Surface tension, viscosity, gravity and evaporation are often incorporated into 1D models (Wong *et al.*, 1996; Sharma *et al.*, 1998; Miller *et al.*, 2002; Braun & Fitt, 2003). Winter *et al.* (2010) improved previous evaporation models by including a conjoining pressure from van der Waals forces that approximated the wettable corneal surface. Incorporating heat transfer from the underlying eye, Li & Braun (2012) resolved a discrepancy of the tear film surface temperature between predictions of existing evaporation models and *in vivo* measurements.

Recently, studies of 1D models that bring together the interblink period and a moving end that represents the upper lid have appeared. Jones *et al.* (2005, 2006) developed models for tear film formation and relaxation that were unified in this way; one end of the domain moved to model the upper lid motion during the opening phase of the blink, and then remained stationary for the subsequent relaxation during the interblink. The tear film was treated as a shear-thinning fluid without elasticity in an otherwise similar model by Jossic *et al.* (2009) to try to tailor the viscosity of eye drops to obtain the most uniform tear film. Braun & King-Smith (2007) modelled eyelid motion for blink cycles by moving one end of the domain sinusoidally and they computed solutions for multiple complete blink cycles. Heryudono *et al.* (2007) followed their study with a more realistic lid motion and specified a flux boundary condition. Good agreement on tear film thickness between experiments and simulations was found by Heryudono *et al.* (2007). Deng *et al.* (2013, 2014) extended the model of Li & Braun (2012) to include upper lid motion (blink) and heat transfer from the underlying eye to explain observed ocular surface temperature measurements and to give new transient temperature results inside the eye. Bruna & Breward (2014) studied a model that added a dynamic lipid layer to an underlying aqueous layer with an insoluble surfactant at the lipid/aqueous interface (representing polar lipids). They computed dynamic results for the model and found various useful limits for it.

Braun (2012) gave a model for a spatially uniform film with no space dependence that was very similar to the one first suggested by King-Smith *et al.* (2007). The original model was a single ordinary differential equation for the tear film thickness that included evaporation from the tear/air interface at a constant rate and osmotic flow from the tear/cornea interface that was proportional to the osmolarity increase above the isotonic value. The latter assumption simplifies the tear/cornea interface to a semi-permeable boundary that allows water but not solutes to pass. They found that the model predicted equilibration of the tear film thickness at values greater than the height of the glycocalyx for sufficiently large permeability of the tear/cornea interface. They also found that the osmolarity could become quite large as the tear film thinned for small permeability values, as much as 10 times the isotonic value under some conditions. The model given in Braun (2012) included van der Waals forces that stopped thinning at the purported height of the glycocalyx which allowed the model to be used at zero permeability at the tear/cornea interface. Similar conclusions about the osmolarity during thinning were found there.

These models were extended to include a specified evaporation profile that varied in space by King-Smith *et al.* (2010b). The evaporation profile was Gaussian with a peak value that could be specified larger than the surrounding constant rate. The local thinning caused by locally increased evaporation led to increased osmolarity in the break-up region, which could be several times larger than the isotonic value. A modified evaporation distribution was created by Peng *et al.* (2014) that had two parts. One part

used an immobile lipid layer with specified thickness and fixed resistance to diffusion through it by water. The other part was a resistance to transport in the air outside the tear film; this second resistance included convective and diffusive transport in the air. They also found that the osmolarity was elevated in this model for break-up.

Zubkov *et al.* (2012) developed a model describing the spatial distribution of tear film osmolarity that incorporates both fluid and solute (osmolarity) dynamics, evaporation, blinking and vertical saccadic eyelid motion. They found that both osmolarity was increased in the black line region and that measurements of the solute concentrations within the lower meniscus need not reflect those elsewhere in the tear film. This model gave results over a line oriented vertically through the centre of the cornea, and thus gave information about the osmolarity over more of the ocular surface than the models mentioned above.

In this paper, we study dynamics of the fluid motion and osmolarity on an eye-shaped domain. To our knowledge, Maki *et al.* (2010a,b) were the first to extend models of fluid dynamics in the tear film to a geometry that approximated the exposed ocular surface. They formulated a relaxation model on a stationary 2D eye-shaped domain that was approximated from a digital photo of an eye. They specified tear film thickness and pressure boundary conditions (Maki *et al.*, 2010a) or flux boundary conditions (Maki *et al.*, 2010b). Their simulations recovered features seen in 1D models such as formation of the black line, and captured some experimental observations of the tear film dynamics around the lid margins. Maki *et al.* (2010b) simplified the *in vivo* mechanisms and imposed a flux boundary condition having only spatial dependence (specifying the location of the lacrimal gland and the puncta holes) in their tear film relaxation model. Under some conditions, they were able to recover hydraulic connectivity as seen experimentally and described above. Li *et al.* (2014) improved the model, added evaporation and a wettable ocular surface, as well as a time-dependent boundary condition that approximated the in- and out-flow of the aqueous layer of the tear film.

In this paper, we formulate a tear film dynamics model on a 2D eye-shaped domain that, adding to the previous models, incorporates osmolarity transport and osmosis from the tear/eye interface. To our knowledge, this is the first such model that includes the osmolarity in a 2D tear film model and that provides a global osmolarity distribution over the entire exposed eye. The permeability of the ocular surface is treated as either constant over the whole surface, or as a space-dependent function with lower permeability over the cornea and higher permeability over the conjunctiva. In the model, the tear film loses water via evaporation to the air, gains water from the ocular surface, and, via the flux boundary condition, has water supplied from the lacrimal gland and removed from the puncta. The model adds significant new results about the distribution of osmolarity over the exposed ocular surface. We believe that these results will impact the understanding of osmolarity dynamics in the tear film as well as the measurement of this important quantity.

We begin by formulating the model in Section 2. A brief description of the numerical methods used for the simulation is discussed in Section 3, followed by detailed results of simulations and comparison with experiments in Section 4. Conclusions and further directions are pointed out in Section 5.

2. Formulation

In this section, we present a mathematical model that incorporates osmolarity and fluid dynamics into a tear film model on a 2D eye-shaped domain as shown in Fig. 1. In Fig. 1, (u', v', w') are the velocity components in the coordinate directions (x', y', z'); z' is directed out of the page and primed variables are dimensional. By g', we denote gravity which is specified in the negative y' direction.

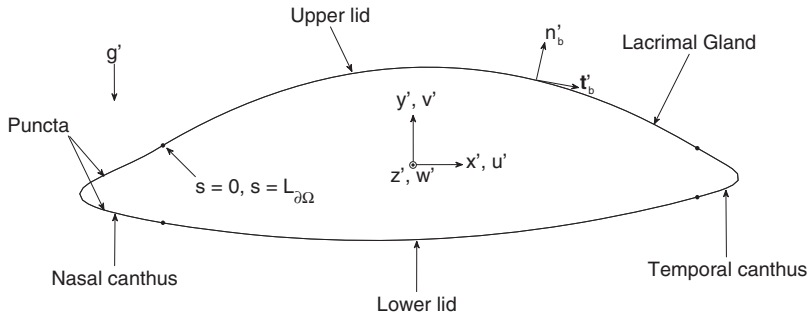

FIG. 1. The coordinate system and eye-shaped domain. The z' direction points out of the page.

The boundary curves of the eye-shaped domain are approximated from a digital photo by four polynomials. Two are parabolas in x' and two are ninth-degree polynomials in y', and C_4 continuity is imposed where they join (indicated by dots) (Maki *et al.*, 2010a,b; Li *et al.*, 2014). By s', we denote the arc length of the boundary starting at the joint of the nasal canthus and upper lid, and is traversed in the counterclockwise direction as s' increases. The unit vectors tangential and normal to the boundary curves are given by $\mathbf{t}'_b$ and $\mathbf{n}'_b$, respectively. By $z' = h'(x', y', t')$, we denote the free surface of the tear film and t' is the time.

We assume that the tear fluid is incompressible and Newtonian with constant density ρ, viscosity μ, specific heat c_p and thermal conductivity k. The tear fluid supplied from the lacrimal gland is more complex than water with salt-ions, containing proteins and other organic molecules (Dartt *et al.*, 2005; Dartt, 2009). Because these large molecules are present in the tear film, whole tears have been found to be shear thinning (Tiffany, 1991), though not strongly so. Similar levels of shear thinning were incorporated by Jossic *et al.* (2009) and though some details change, the qualitative features of the flow and thickness distribution are, for our purposes here, similar to the Newtonian case. More recently, meibum (secreted from the glands in the eyelids) has been found to introduce elasticity into the tear film when temperature is below 32°C (Leiske *et al.*, 2011). Note that viscoelastic surfactants can affect film stability in a model system (Rosenfeld & Fuller, 2012). However, it is not yet clear how these measurements affect overall tear film properties at typical *in vivo* operating temperatures that are often near 35°C (Efron *et al.*, 1989). Because our current knowledge indicates that the shear thinning of the tear film is not strong (Tiffany, 1991) and because viscoelastic surface effects appear to be small at *in vivo* temperatures (Leiske *et al.*, 2012), we make the simplifying assumption of constant properties.

We also assume the ocular surface is flat due to the fact that the characteristic thickness of the human tear film is much less than the radius of curvature of the ocular globe (Berger & Corrsin, 1974; Braun *et al.*, 2012). The governing equations for the tear film thickness $h'(x', y', t')$ and the osmolarity $c'(x', y', t')$ are derived from the incompressible Navier–Stokes and convection–diffusion equations, respectively. The two equations are coupled by the osmotic flux, that is, the fluid that flows from the ocular surface at $z' = 0$ into the tear film driven by the osmolarity difference between the tear film and the cornea (Levin & Verkman, 2004). In the model, water is lost to the air, treated as a passive gas outside the tear film ($z' > h'$), and water is supplied due to the subsequent increased osmolarity via this osmotic flux.

After non-dimensionalization and simplification using lubrication theory (e.g. Jensen & Grotberg, 1993; Braun, 2012), we arrive at a system of partial differential equations (PDEs) for the dimensionless

variables $h(x, y, t)$ and $c(x, y, t)$:

$$\partial_t h + EJ + \nabla \cdot \mathbf{Q} - P_c(c-1) = 0, \tag{2.1}$$

$$h\partial_t c + \nabla c \cdot \mathbf{Q} = EcJ + \frac{1}{\mathrm{Pe}_c}\nabla \cdot (h\nabla c) - P_c(c-1)c. \tag{2.2}$$

The evaporative mass flux J is given by

$$J = \frac{1 - \delta(S\Delta h + Ah^{-3})}{\bar{K} + h},$$

and the fluid flux $\mathbf{Q}$ across any cross-section of the film is given by

$$\mathbf{Q} = \frac{h^3}{12}\nabla(S\Delta h + Ah^{-3} - Gy).$$

The conjoining pressure in modelling evaporation plays an important role in the tear film model. It is meant to mimic the effect of the glycocalyx, whose transmembrane are strongly wet by water and we assume that they arrest the thinning of the tear film. A secondary benefit is that the model allows solutions to be computed past the initial tear film break-up because the tear film thickness never reaches zero in this model. These aspects of evaporation competing with conjoining pressure are discussed by Winter *et al.* (2010) in the context of eyes, but the idea was developed by Potash & Wayner (1972) and Moosman & Homsy (1980). More recent versions of the approach may be found in Morris (2001) and Ajaev & Homsy (2001). The non-dimensional parameters that arise are defined and given values in the following section and in Table 1. The dimensional parameters used in those expressions are given in Table 2. A detailed derivation of the governing Equations (2.1) and (2.2) can be found in Appendix A.

2.1 *Parameter descriptions*

Lubrication theory exploits the small value of ϵ, which is the ratio of the tear film thickness to the length scale along the tear film; E characterizes the evaporative contribution to the surface motion, δ measures the pressure influence to evaporation, S is the ratio of surface tension to viscous forces, A is the Hamaker constant in non-dimensional form related to the unretarded van der Waals force, G is the ratio of gravity to the viscous force, $\bar{K}$ represents the non-equilibrium parameter that sets the evaporative mass flux, Pe_c is the Péclet number for the osmolarity describing the competition between convection and diffusion and P_c is the water permeability of the ocular surface (P_{corn} and P_{conj} specify the values of P_c over the cornea and conjunctiva, respectively).

Evaporation makes major contributions to tear film thinning between blinks (Kimball *et al.*, 2010 and references therein) and increases the osmolarity of tears, which in turn induces an osmotic flow through the ocular surface that compensates for much of the evaporative water loss. Nichols *et al.* (2005) have found that the mean rate of thinning of the pre-cornea tear film is $3.79 \pm 4.20\,\mu$m/min, and the histogram of their measurements shows an asymmetrical distribution, with narrow peaks corresponding to a thinning rate of $\sim$1 μm/min but with many instances of much more rapid thinning (King-Smith *et al.*, 2010a, as well). Based on these experimental measurements, we tune the non-equilibrium parameter $\bar{K}$ that sets the evaporative mass flux such that the thinning rate of the flat tear film (i.e. neglecting all the spatial derivatives) is 4 μm/min. The model does not take into account transport or the relative humidity outside the tear film as in Peng *et al.* (2014); it is suitable for controlled laboratory conditions.

TABLE 1 *Dimensionless parameters. Values and descriptions of the dimensional parameters appeared are given in Table 2.*

Parameter	Expression	Value
ϵ	$\frac{d'}{L'}$	1×10^{-3}
E	$\frac{k(T'_B - T'_s)}{d'\mathcal{L}_m \epsilon \rho U_0}$	118.3
S	$\frac{\sigma \epsilon^3}{\mu U_0}$	6.92×10^{-6}
$\bar{K}$	$\frac{kK}{d'\mathcal{L}_m}$	8.9×10^{3}
G	$\frac{\rho g (d')^2}{\mu U_0}$	0.05
δ	$\frac{\alpha \mu U_0}{\epsilon^2 L'(T'_B - T'_s)}$	4.66
A	$\frac{A^*}{L' d \mu U_0}$	2.14×10^{-6}
Pe_c	$\frac{U_0 L'}{D_c}$	9.62×10^{3}
P_{corn}	$\frac{P_{\mathrm{corn}}^{\mathrm{tiss}} v_w c_0}{\epsilon U_0}$	0.013
P_{conj}	$\frac{P_{\mathrm{conj}}^{\mathrm{tiss}} v_w c_0}{\epsilon U_0}$	0.06

2.2 *Permeability of the ocular surface*

The ocular surface is believed to be permeable, and the induced osmotic flow helps to arrest tear film thinning and hence ameliorate osmolarity elevation (Braun, 2012). In addition, the water permeability over the ocular surface is not a constant; the conjunctiva is normally more permeable than the cornea (Dartt, 2002). King-Smith and coworkers proposed values for the water permeability of the ocular surface, that is, 12.0 μm/s for the cornea and 55.4 μm/s for the conjunctiva (King-Smith *et al.*, 2010b; Bruhns *et al.*, 2014). We use these values to determine the dimensionless permeability P_c in the model as follows: we first define the corneal region as a unit circle with the centre $\mathbf{X_c} = (0.05, 0.225)$ in the domain shown in Fig. 1, and the variable permeability at any position $\mathbf{X} = (x, y)$ is then defined as

$$P_c(x, y) = \frac{P_{\mathrm{conj}} - P_{\mathrm{corn}}}{2} \tanh\left(\frac{|\mathbf{X} - \mathbf{X_c}| - 1}{x_0}\right) + \frac{P_{\mathrm{conj}} + P_{\mathrm{corn}}}{2}. \tag{2.3}$$

Here $P_{\mathrm{conj}} = 0.06$ is the dimensionless permeability of conjunctiva, $P_{\mathrm{corn}} = 0.013$ is the dimensionless permeability of cornea and $|\mathbf{X} - \mathbf{X_c}|$ is the distance between points $\mathbf{X}$ and $\mathbf{X_c}$. Here x_0 is the width of the transition between the different permeabilities. We typically used $x_0 = 0.05$ which corresponds

TABLE 2 *Dimensional parameters.*

Parameter	Description	Value	Reference
μ	Viscosity	1.3×10^{-3} Pa·s	Tiffany (1991)
σ	Surface tension	0.045 N·m^{-1}	Nagyová & Tiffany (1999)
k	Tear film thermal conductivity	0.68 W·m^{-1}·K^{-1}	Water
ρ	Density	10^3 kg·m^{-3}	Water
$\mathcal{L}_m$	Latent heat of vaporization	2.3×10^6 J·kg^{-1}	Water
T_s'	Saturation temperature	27°C	Estimated
T_B'	Body temperature	37°C	Estimated
g	Gravitational acceleration	9.81 m·s^{-2}	Estimated
A^*	Hamaker constant	3.5×10^{-19} Pa·m^3	Winter *et al.* (2010)
α	Pressure coefficient for evaporation	3.6×10^{-2} K·Pa^{-1}	Winter *et al.* (2010)
K	Non-equilibrium coefficient	1.5×10^5 K·m^2·s·kg^{-1}	Estimated
d'	Characteristic thickness	5×10^{-6} m	King-Smith *et al.* (2004)
L'	Half-width of palpebral fissure	5×10^{-3} m	Estimated
U_0	Characteristic speed	5×10^{-3} m/s	King-Smith *et al.* (2009)
$P_{\text{corn}}^{\text{tiss}}$	Tissue permeability of cornea	12.0 μm/s	King-Smith *et al.* (2010b)
$P_{\text{conj}}^{\text{tiss}}$	Tissue permeability of conjunctiva	55.4 μm/s	King-Smith *et al.* (2010b)
v_w	Molar volume of water	1.8×10^{-5} m^3·mol^{-1}	Water
D_c	Diffusivity of osmolarity in water	2.6×10^{-9} m^2/s	Zubkov *et al.* (2012)

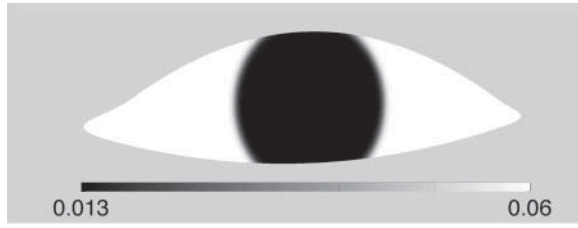

FIG. 2. Variable permeability distribution over the ocular surface with $x_0 = 0.05$.

to a physically realistic value of 0.25 mm dimensionally. We found that the results were insensitive to changes in x_0 around this value. Figure 2 plots the distribution of the variable permeability on the eye-shaped domain.

2.3 *Boundary conditions*

Along the boundary of the eye-shaped domain (denoted as $\partial\Omega$), we prescribe the constant tear film thickness

$$h|_{\partial\Omega} = h_0. \tag{2.4}$$

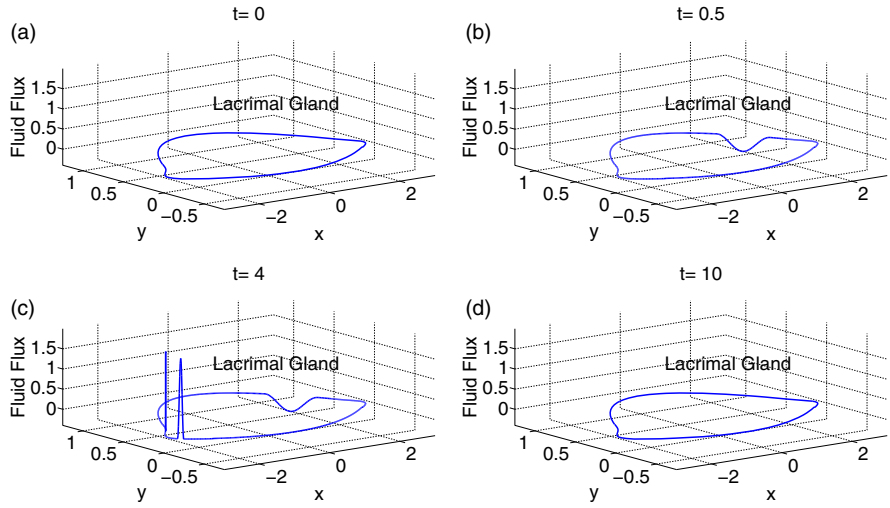

FIG. 3. Time sequences of fluid flux boundary condition during one flux cycle.

We set $h_0 = 13$ in the computation because this choice is in the range of experimental measurement (48–66 μm or 9.6–13.2 non-dimensionally) from Golding *et al.* (1997). In addition, we specify the normal component of the fluid flux,

$$\mathbf{Q} \cdot \mathbf{n}_b = Q_{lg}(s,t) + Q_p(s,t), \tag{2.5}$$

according to the mechanism of Doane (1981) for tear supply and drainage, and the tear drainage model of Zhu & Chauhan (2005), but with simplification regarding blinking. This fluid flux boundary condition mimics some effects of blinking by providing a time-dependent influx through the lacrimal gland and efflux through the puncta. Specifically, the lacrimal gland supply turns on at the beginning of a flux cycle, and the punctal drainage follows one time unit later. Both the supply and drainage start to shut off at $t = 5$. The duration of a complete flux cycle in the model is $\Delta t_{bc} = 10$. In Fig. 3, we show a sequence of images of the fluid flux boundary condition (2.5) within a flux cycle. At $t = 0$ (Fig. 3a), there is zero fluid flux on the boundary. At $t = 0.5$, we see that the lacrimal gland supply is fully on while the drainage does not yet start in Fig. 3b; the drainage begins at $t = 1$. In Fig. 3c, both supply at the lacrimal gland and drainage at the two puncta holes remain fully on. Then, the fluid flux turns off at $t = 5$ and remains zero until the end of a flux cycle ($t = 10$) as shown in Fig. 3d. The influx and efflux are balanced in each flux cycle. See Appendix B and Li *et al.* (2014) for the detailed formula and a supplementary movie for the time-dependent flux boundary condition (2.5).

For the osmolarity $c(x, y, t)$, we consider two limiting cases for the boundary conditions in this paper. Case (i) is the Dirichlet boundary condition

$$c|_{\partial\Omega} = 1; \tag{2.6}$$

this represents perfect exchange between the tear film and idealized isotonic tear fluid supply under the lids (in the fornices). Case (ii) is the homogeneous Neumann boundary condition

$$\nabla c \cdot \mathbf{n}_b|_{\partial\Omega} = 0; \tag{2.7}$$

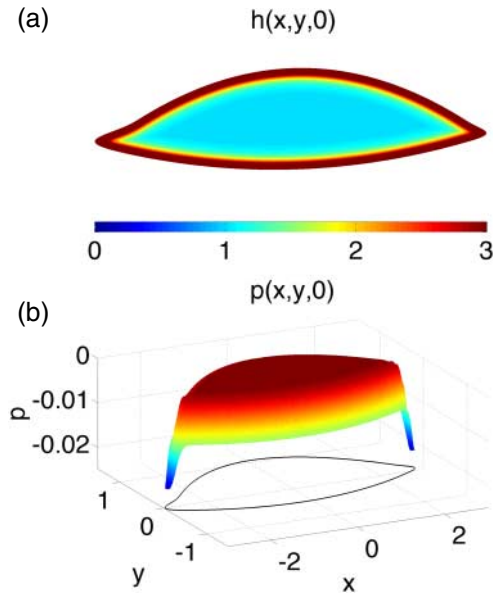

FIG. 4. Smoothed initial conditions for h and p. (a) Initial tear film thickness. The band around the outer edge indicates tear film thickness $h \geqslant 3$. (b) Initial pressure distribution.

this case represents a complete lack of exchange of osmolarity between the tear film and the tear fluid under in the fornices. In the results that we have computed, the results are quite similar for these two cases; this fact will be discussed further in Section 4.

2.4 *Initial condition*

The initial condition $h(x, y, 0)$ is specified based on a numerically smoothed version of the function

$$h(x, y, 0) = 1 + (h_0 - 1)\, \mathrm{e}^{-\min(\mathrm{dist}((x,y),\partial\Omega))/x_0}, \tag{2.8}$$

where $x_0 = 0.06$ and $\mathrm{dist}(\mathbf{X}, \partial\Omega)$ is the distance between a point with position vector $\mathbf{X}$ and a point on the boundary $\partial\Omega$ (Maki *et al.*, 2010a,b). It specifies a dimensional initial volume of about 1.805 μl. This value is well within the experimental measurements by Mathers & Daley (1996), who found the volume of exposed tear fluid to be 2.23 ± 2.5 μl. The initial pressure $p(x, y, 0)$ is calculated from Equation (3.2) accordingly (Li *et al.*, 2014). Figure 4 shows the initial thickness h and pressure p that are implemented in the numerical simulations. For the initial osmolarity, we assume the salt-ions are well mixed and of the isosmotic physiological salt concentration (302 $\mathrm{Osm/m^3}$, or 1 nondimensionally) at the beginning, thereby specifying

$$c(x, y, 0) = 1. \tag{2.9}$$

3. Numerical methods

For numerical purposes, we rewrite the model equations by introducing the pressure $p(x, y, t)$ as a new dependent variable:

$$\partial_t h + E\frac{1+\delta p}{\bar{K}+h} + \nabla\cdot\left[-\frac{h^3}{12}\nabla(p+Gy)\right] - P_c(c-1) = 0, \tag{3.1}$$

$$p + S\Delta h + Ah^{-3} = 0, \tag{3.2}$$

$$h\partial_t c + \nabla c\cdot\left[-\frac{h^3}{12}\nabla(p+Gy)\right] = Ec\frac{1+\delta p}{\bar{K}+h} + \frac{1}{\mathrm{Pe}_c}\nabla\cdot(h\nabla c) - P_c(c-1)c. \tag{3.3}$$

The corresponding boundary conditions must be applied: (2.4), (2.5) and one of (2.6) or (2.7). Note that the flux condition (2.5) is readily converted into a Neumann condition on p. The initial conditions must be applied as well, using smoothed versions of (2.8) and (3.2), as well as (2.9).

We solve the Equations (3.1–3.3) on the eye-shaped geometry (Fig. 1) using the Overture computational framework (http://www.overtureframework.org, Last accessed 24 March 2015. Primary developer and contact: W. D. Henshaw, henshw@rpi.edu), which is a collection of C++ libraries for solving PDEs on complex domains (Chesshire & Henshaw, 1990; Henshaw, 2002).

3.1 *Computational grid*

The tear film is relatively thin and flat in most of the interior of the exposed ocular surface; the thickness increases rapidly near the eyelids forming relatively steep menisci around the boundary of corresponding computational domain. In order to solve the tear film model efficiently, we use five component grids, whose union is the computational grid. The component grids are one Cartesian background grid that has grid lines aligned with the coordinate axes, and four boundary-fitted grids near the boundary. The solution values are interpolated between grids where they overlap. We generated a new computational grid using the grid generation capabilities of the Overture computational framework. We extend the boundary-fitting grids from the boundary using transfinite interpolation, which is a generalized shearing transformation that maps the unit square onto the region bounded by four curves (Chesshire & Henshaw, 1990; Henshaw, 2002). Unlike grids based on extending normals from the boundary, we can extend the boundary-fitting grids as much as we want without worrying about intersecting normal lines. This provides us with the boundary-fitting grids that are wide enough to cover the menisci of the tear film. In addition, we double the grid spacing for the background Cartesian grid to reduce the number of grid points compared with previous work (Maki *et al.*, 2010a,b; Li *et al.*, 2014). The new grid, plotted in Fig. 5, reduces the total number of grid points by about 14% while achieving better overall accuracy for test problems (the new grid has a total number of 235,018 grid points). Unless otherwise noted, all the simulation results presented in this paper are computed using the computational grid in Fig. 5.

3.2 *A hybrid time-stepping scheme*

To solve the Equations (3.1–3.3), we first discretize the spatial derivatives using the second-order accurate finite difference method for curvilinear and Cartesian grids from Overture. Since the model Equations (3.1–3.3) are weakly coupled by osmosis (terms involving P_c), we developed a hybrid time-stepping scheme to solve the coupled system: we first solve the Equation (3.3) for c using a dynamic explicit Runge–Kutta–Chebyshev (RKC) method (Sommeijer *et al.*, 1997); then we update the h and p

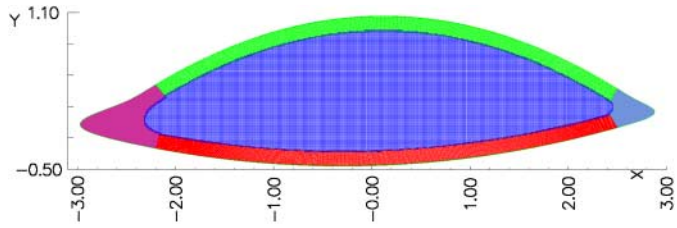

FIG. 5. Computational grid on the eye-shaped domain.

Equations (3.1) and (3.2) and solve them using the variable step size backward differentiation formula (BDF) method with fixed leading coefficient based on Brenan *et al.* (1996) and Maki *et al.* (2010a,b). The resulting non-linear system of the BDF method is solved using Newton's iteration method. Solutions on different component grids are coupled by interpolation. The RKC method is suitable for this problem because it has an extended stability region with a stability bound that is quadratic in the number of stages, and the explicit method is fast and easy to implement. We exploit the non-linear power method for an estimation of the largest eigenvalue of the spatially discretized system from (3.3) for c, and we use the quadratic relation to determine the number of stages needed for the RKC method. We have empirical criteria to determine whether an approximation is accepted or not. The number of stages is updated at every successful time step. More detailed results regarding the numerical analysis and performance of this method will appear elsewhere, since our focus is on the tear film here.

4. Results

In this section, we present computed results for the tear film thickness $h(x, y, t)$ and the osmolarity $c(x, y, t)$ on the 2D eye-shaped domain. We vary the water permeability P_c and the thinning rate (evaporation) that sets the non-equilibrium parameter $\bar{K}$ to study their influence on the dynamics of both tear film and osmolarity. We also explore two types of boundary condition for the osmolarity $c(x, y, t)$: (i) Dirichlet, given by (2.6), and (ii) homogeneous Neumann, given by (2.7).

4.1 *Constant non-zero permeability*

We begin by presenting results for the model with the same constant water permeability over the whole ocular surface; we use the corneal permeability corresponding to $P_c = 0.013$ measured by King-Smith *et al.* (2010b) and Bruhns *et al.* (2014). Figure 6 shows the contours of the simulation results. The left column represents the tear film thickness, and the right column represents the osmolarity. We see the dark band (blue online) set inside of the boundary, representing the so-called black line, emerges rapidly near to and inside of the menisci in the left column. The black line develops due to capillary action resulting from the positive curvature of the menisci generating a low pressure that sucks fluid into the meniscus. A local minimum thus forms near the meniscus, and is referred to as the black line. In addition, the canthi in the 2D eye-shaped domain induce a second direction of curvature, creating an even lower pressure that attracts fluid towards themselves. Therefore, the tear film near the two canthi is often thinner than other parts of the black line. In this case, the global minimum is located near the nasal canthus, which is sharper (more curved) than the temporal canthus. The formation of the global minimum is also promoted by the efflux of fluid near the nasal canthus due to the boundary conditions that mimic punctal drainage from this region. This also shows that both the thickness and

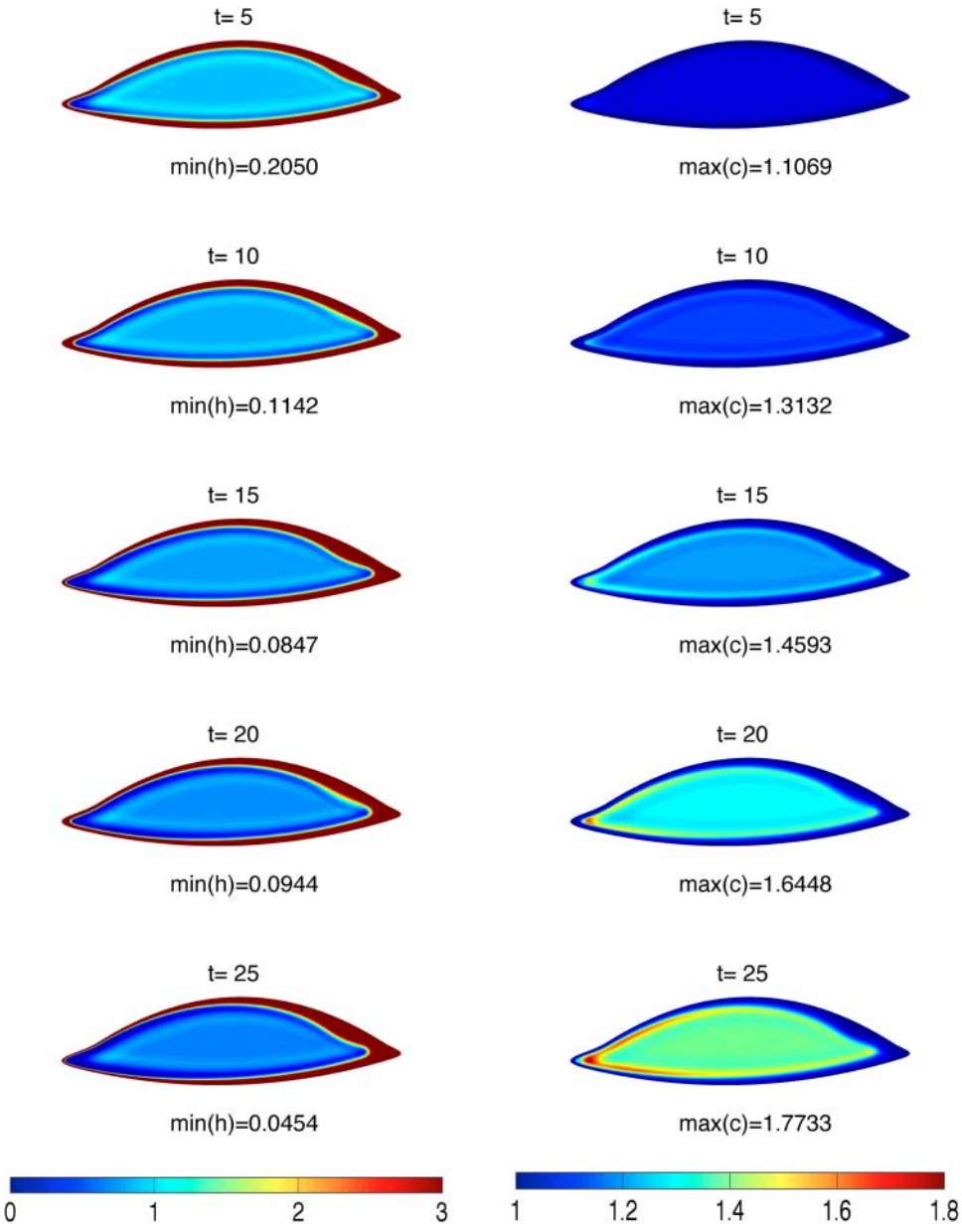

FIG. 6. Contours of tear film thickness (left column) and osmolarity (right column) with constant permeability of $P_c = 0.013$ all over the exposed ocular surface and with Dirichlet boundary condition (2.6) on the osmolarity. The thinning rate is 4 μm/min.

osmolarity vary significantly away from the vertical line through the centre of the cornea. Note 1D models formulated along this line do not account for this variation. The redistribution of fluid due to surface tension also causes a small ridge to form on the interior side of the black line. This is seen as a diffuse light band in the left column of Fig. 6. This light band is a ridge that has been seen in a

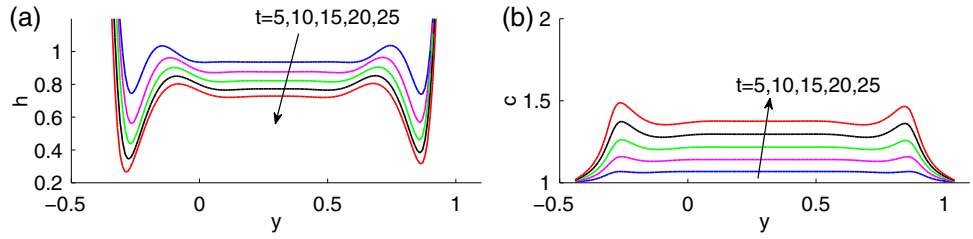

FIG. 7. Cross-sectional plots through the vertical line $x = 0$ with $P_c = 0.013$ and Dirichlet boundary condition (2.6). The thinning rate is 4 μm/min and the upper eyelid is located on the positive side of the y-axis. (a) Tear film thickness. (b) Osmolarity.

number of other studies (Maki *et al.*, 2010a,b; Li *et al.*, 2014). The tear film thickness in the interior decreases steadily throughout the computation because of evaporation; this is visualized by the continual darkening of the interior in the contour plots.

The corresponding osmolarity contours are plotted in the right column of Fig. 6. Generally, the osmolarity increases more where the tear film is thinner, such as in the black line and canthi regions. This is in qualitative agreement with the results of Zubkov *et al.* (2012); we return to a direct comparison with their 1D results for $P_c = 0$ in the next section. The global maximum of osmolarity is in the nasal canthus that corresponds to the location of thinnest tear film. In the osmolarity plots, we observe a bright band indicating that a region of elevated osmolarity is forming near the developing black line. Osmolarity in the interior continues to increase as a result of evaporation, and the interior of the eye-shaped domain becomes brighter in the plots. In the region where the tear film forms a small ridge, a corresponding darker band is also present on the interior side of the brighter band in the osmolarity plots.

The vertical cross-sectional plots ($x = 0$), shown in Fig. 7, illustrate more directly the correlation between the tear film thickness and osmolarity: the osmolarity is roughly the reciprocal of the tear film thickness except in the black line and meniscus regions. Furthermore, comparison with the zero permeability case in the next section also reveals the effects of osmosis: the tear film is slightly thicker while the osmolarity is obviously smaller for the constant non-zero permeability case.

4.2 *Zero permeability*

Now, we consider our model on an impermeable ocular surface, i.e. $P_c = 0$, so as to reveal the effect of osmosis by comparing with the previous results in Section 4.1, and we make comparisons with existing studies on 1D domains to show that our model provides consistent predictions. In this case, no water is supplied in response to the increased osmolarity that occurs when water evaporates from the tear film. Figure 8 shows the contours of both tear film thickness and osmolarity on the eye-shaped domain at $t = 25$. It shows that both the thickness and osmolarity vary significantly away from the vertical line through the centre of the cornea. For example, the global minimum of tear film thickness is located in the nasal canthus and is much smaller than that in the cross-sectional plot. Furthermore, there is a spike in the osmolarity contour with a global maximum as large as $\max(c) = 4.8031$ in the nasal canthus. These global extrema and their locations cannot be found via 1D models, and to our knowledge are not available from clinical measurements either. From Fig. 8, we also see more elevated osmolarity at the black line region, and the lowest concentration is located near the lacrimal gland as a result of the fresh tear supply. The tear film dynamics predicted by this model are in agreement with previous results (Li *et al.*, 2014).

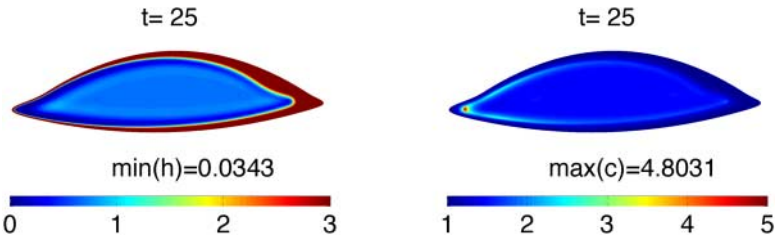

FIG. 8. Contours of tear film thickness (left) and osmolarity (right) with $P_c = 0$ and Dirichlet boundary condition (2.6). The thinning rate is 4 μm/min.

TABLE 3 *Extreme values for various cases*; $P_c(x, y)$ *denotes the variable permeability case and is given by Equation* (2.3).

	Thinning rate:	4 μm/min		10 μm/min	20 μm/min
	$P_c = 0$	$P_c = 0.013$	$P_c(x, y)$	$P_c(x, y)$	$P_c(x, y)$
$\min(h(x, y, 5))$	0.2043	0.2050	0.2070	0.1880	0.1557
$\min(h(x, y, 10))$	0.1072	0.1142	0.1294	0.1102	0.0931
$\min(h(x, y, 15))$	0.0819	0.0847	0.0899	0.0722	0.0506
$\min(h(x, y, 20))$	0.0716	0.0944	0.1118	0.0906	0.0471
$\min(h(x, y, 25))$	0.0343	0.0454	0.0492	0.0382	0.0268
$\max(c(x, y, 5))$	1.1135	1.1069	1.0873	1.2392	1.5629
$\max(c(x, y, 10))$	1.3925	1.3132	1.1722	1.5091	2.7505
$\max(c(x, y, 15))$	1.6975	1.4593	1.2673	1.9892	5.3456
$\max(c(x, y, 20))$	2.4841	1.6448	1.3852	2.6045	5.9684
$\max(c(x, y, 25))$	4.8031	1.7733	1.5124	3.1486	6.0538

The effect of osmosis can be readily seen by comparing the extreme values of different permeability cases. The extreme values of both h and c for several cases we considered in this paper are listed in Table 3. For the constant non-zero permeability case ($P_c = 0.013$), the minimum thickness ($\min(h) = 0.0454$) is slightly larger than that with zero permeability ($\min(h) = 0.0343$) at $t = 25$. However, the peak of osmolarity is significantly reduced by osmotic flows: $\max(c) = 1.7733$ with constant permeability and $\max(c) = 4.8031$ with zero permeability at $t = 25$. Therefore, according to our computation, we conclude that the presence of osmotic flux across the corneal surface may protect the tear film from excessive hyperosmolarity which could cause damage to the ocular surface and/or denaturation of tear film mucins and proteins (Govindarajan & Gipson, 2010).

Zubkov *et al.* (2012) studied a system that included both tear film and osmolarity dynamics on a 1D domain with a moving end that mimicked blinks; their model assumes that the ocular surface is impermeable. To compare with their model, we set $P_c = 0$ and show the cross-sectional plots through the vertical line $x = 0$; the results are in Fig. 9. The cross-sectional curves of our results on the 2D eye-shaped domain are comparable to the 1D results of Zubkov *et al.* (2012) during the interblink phase for both the tear film thickness (Fig. 9a) and the osmolarity distribution (Fig. 9b), except that the development of the black line is slower and the maximum osmolarity is higher in our results. The slower development of the black line in our results is due to the stationary domain, because the formation of the black line begins during the opening phase according to previous results on 1D blinking domains

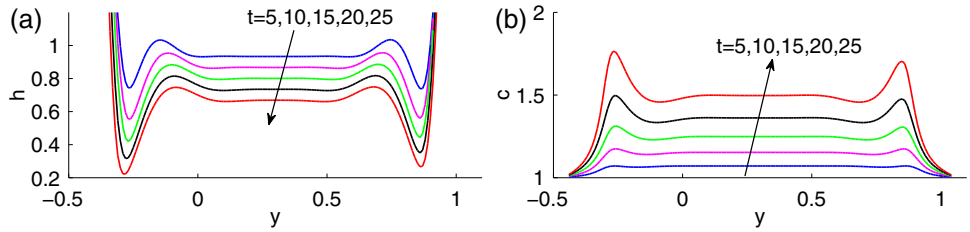

FIG. 9. Cross-sectional plots through the vertical line $x = 0$ with $P_c = 0$ and Dirichlet boundary condition (2.6). The thinning rate is 4 μm/min and the upper eyelid is on the positive side of the y-axis. (a) Tear film thickness. (b) Osmolarity.

(Jones *et al.*, 2005; Braun & King-Smith, 2007; Heryudono *et al.*, 2007; Maki *et al.*, 2008; Zubkov *et al.*, 2012). Nevertheless, the behaviour of the tear film thickness in our model is in line with many previous results of 1D models with stationary ends (Braun & Fitt, 2003; Winter *et al.*, 2010; Li & Braun, 2012). The difference between the values of osmolarity stemmed from the different assumptions of the thinning rate and our longer time for computing the solution. The thinning rate in the model of Zubkov *et al.* (2012) is assumed to be 0.24 μm/min, which is much smaller than most of the observations of Nichols *et al.* (2005) and our choice of 4 μm/min. Zubkov *et al.* have also considered various evaporation rates to deduce that evaporation increases osmolarity, and they computed results for only 5 s, which explains the larger values of osmolarity we obtain as shown in Fig. 9b.

4.3 *Variable permeability*

In this section, we present simulated results by specifying the variable permeability $P_c(x, y)$ as defined in Equation (2.3). Figure 10 shows time sequences of the contours for both tear film thickness (left column) and osmolarity distribution (right column). Most of the dynamics of tear film thickness are similar to previous cases, such as the development of the black line and the continuously thinning in the interior as a result of evaporation. However, due to the variable permeability of the ocular surface, we observe different patterns of tear film thickness over the conjunctival region and the corneal region in the left column of Fig. 10. Since the cornea is less permeable, we see in the thickness plots that the tear film is thinner in the corneal region; it appears as a darker (blue) island in the centre of the eye-shaped domain.

For the osmolarity distribution shown in the right column of Fig. 10, several new patterns are observed beyond the elevated osmolarity in the black line region and the increasing of osmolarity due to evaporation. Because the cornea is less permeable than the conjunctiva, less osmotic flow is expected through the cornea, and this expectation is clearly captured by the model. In the osmolarity contours in Fig. 10, we can clearly see a brighter disc in the region of cornea indicating higher osmolarity there. Combining the effect of surface tension and evaporation, the osmolarity is even larger in the black line region over the cornea, and the global maximum of osmolarity is attained there. Comparing with the constant permeability case, both $\min(h)$ and $\max(c)$ are slightly changed since, in the variable permeability case, we have a more permeable conjunctiva.

In order to better observe the transition from conjunctiva to cornea, we plot the horizontal cross-sectional plots (through the line $y = 0.3$ which is roughly across the geometric centre of the cornea (GCC)) in Fig. 11. Because of the punctal drainage and lacrimal gland supply specified by the time-dependent fluid flux boundary condition (2.5), the tear film thickness is much smaller for $x < 0$ in Fig. 11a. A local minimum of the tear film thickness, or black line, is still observed in the canthus regions

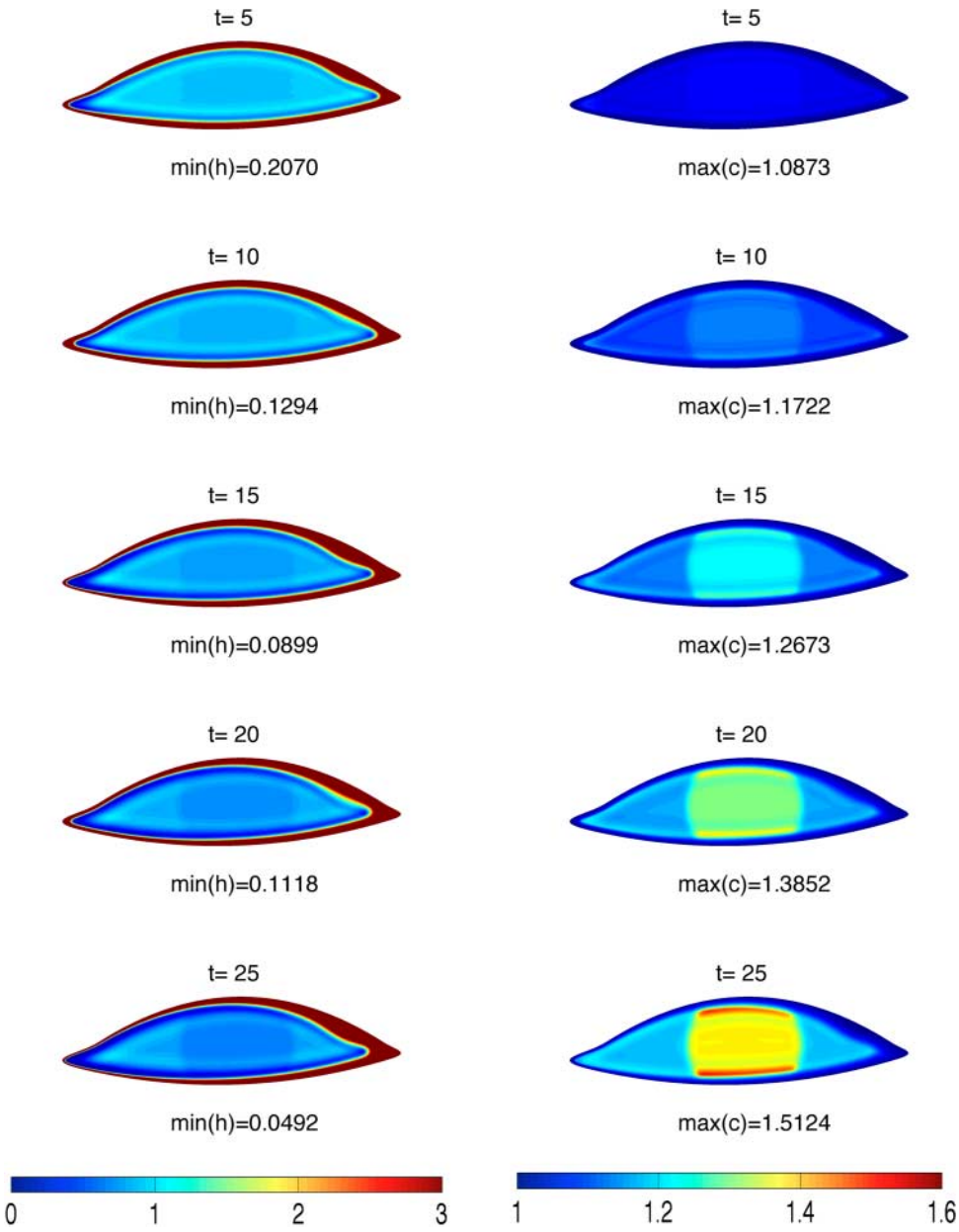

FIG. 10. Contours of tear film thickness (left column) and osmolarity (right column) with variable permeability (2.3) and Dirichlet boundary condition (2.6). The thinning rate is 4 μm/min.

due to the curvature of the menisci. The abrupt change of permeability from conjunctiva to cornea is reflected by the tear film thickness. In Fig. 11a, we see a rapid drop of tear film thickness around $x = \pm 1$ near the boundary of the cornea. The transition of permeability influences the osmolarity distribution

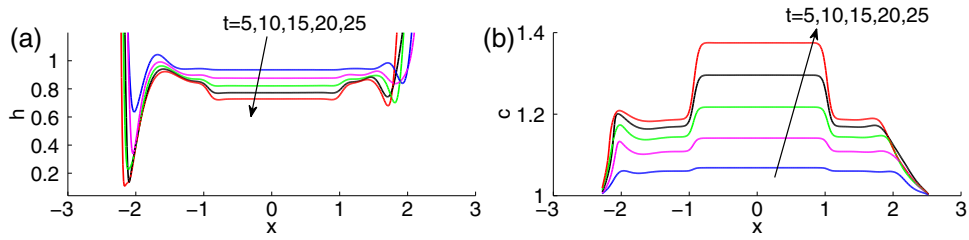

FIG. 11. Cross-sectional plots through the horizontal line $y = 0.3$ with variable permeability (2.3) and Dirichlet boundary condition (2.6). Thinning rate is 4 μm/min and the temporal canthus is located at the positive side of the x-axis. (a) Tear film thickness. (b) Osmolarity.

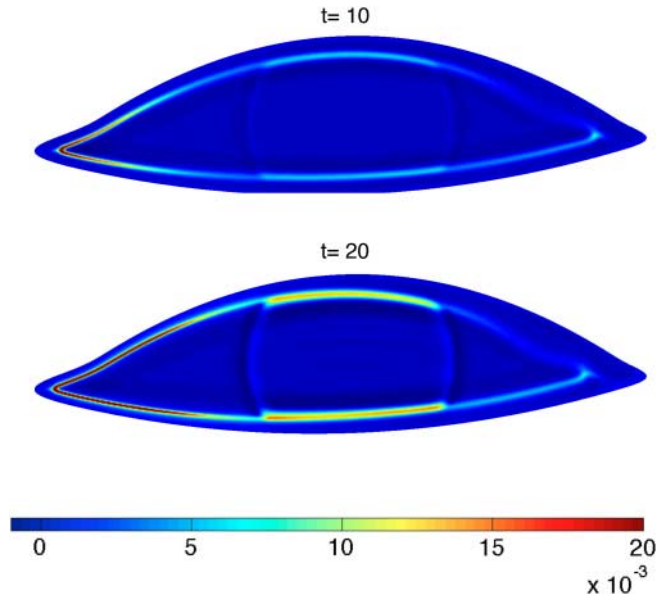

FIG. 12. The contribution of diffusion to osmolarity dynamics. Diffusion is larger (magnitude $> 10^{-2}$) in the lighter areas.

even more dramatically. After $t = 10$, the osmolarity in the cornea surpasses the osmolarity in the nasal canthus (the location of global peak of osmolarity for the zero and constant permeability cases).

4.3.1 *Diffusion* Diffusion also plays a role in the osmolarity dynamics. In Figure 12, we plot the diffusive term, $-[\nabla \cdot (h\nabla c)]/(h\mathrm{Pe}_c)$, in the c equation over the eye-shaped geometry to investigate its influence on the whole model system. From Fig. 12, we see that the diffusion is non-negligible (indicated by the lighter colours and the magnitude is $> 10^{-2}$) inside the black line regions; diffusion is actually of the same size as advection in the black line regions at $t = 20$. Our direct plots of the diffusion term on the eye-shaped domain confirmed the results on the 1D domain of Zubkov *et al.* (2012), who studied diffusion by comparing computed results for models with and without diffusivity. Even though the Pèclet number is large in the model system, diffusion helps to ameliorate the high osmolarity level

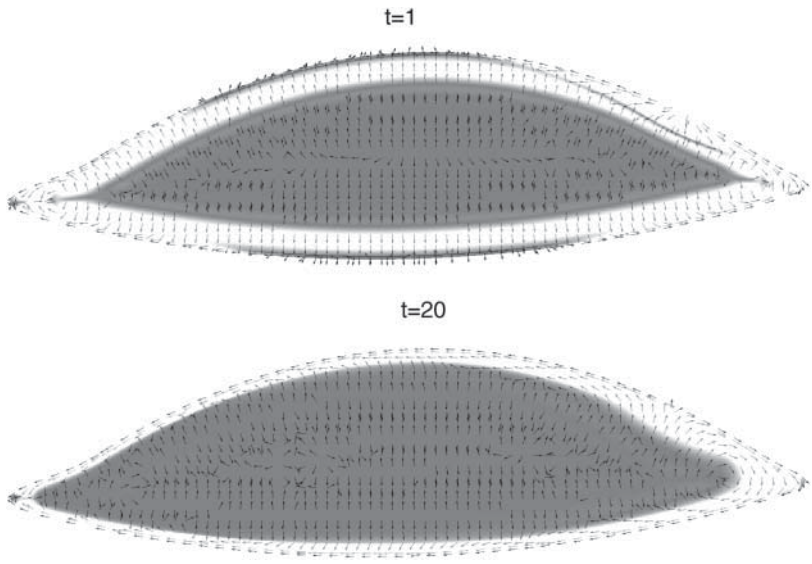

FIG. 13. Fluid flux (**Q**) over contours of its magnitude with variable permeability and thinning rate 4 μm/min. (Far fewer arrows than the computational grid points are shown for clarity. All the arrows in this plot start at different locations.)

in the black line regions. Diffusion could affect the osmolarity distribution similarly in local spots of break-up (Peng *et al.*, 2014).

4.3.2 *Movement of fluid and solutes* Figure 13 shows the quiver plots of the fluid flux **Q** at time $t = 1$ and $t = 20$. The normalized arrows in the plots show the directions only, and we use the shading to indicate the magnitude of the flux vector: the darker the background, the smaller is the flux. In particular, white indicates a flux $> 10^{-2}$; dark grey is $< 10^{-3}$. At $t = 1$, the formation of the black line dominates the movement of tear fluid. We see from the first plot of Fig. 13 that relatively fast flow ($\|\mathbf{Q}\| \geqslant 10^{-2}$) is observed near the menisci, and all the arrows pointing towards the eye lids. This is because the lower pressure created by the menisci attracts the nearby fluid forming a locally thin region. This thin region is referred to as the black line and corresponds to the dark blue band as we pointed out in the thickness contour plots previously. In the second plots of Fig. 13, relatively fast fluid motion ($\|\mathbf{Q}\| \geqslant 10^{-2}$) still occurs in the menisci; however, the arrows in the menisci show that the flow splits near the lacrimal gland and moves towards the nasal canthus along the eye lids. This hydraulic connectivity is thought to be caused by the pressure difference created by the time-dependent influx and efflux on the boundary. The pressure gradient in the menisci drives the fluid flows towards the nasal side.

Li *et al.* (2014) have studied tear flow over the eye-shaped geometry specifying the same time-dependent flux BC (2.5). They discovered that, after the development of the black line, relatively fast fluid flow occurs in the menisci corresponding to the experimentally observed hydraulic connectivity, while, on the inner side of the black line region, fluid flow is small. The model in this paper couples the fluid dynamics in the tear film with the osmolarity and still captures hydraulic connectivity.

The model Equations (2.1) and (2.2) can be combined into a single PDE (Peng *et al.*, 2014):

$$\partial_t(ch) + \nabla \cdot \left(c\mathbf{Q} - \frac{h}{Pe_c}\nabla c \right) = 0. \tag{4.1}$$

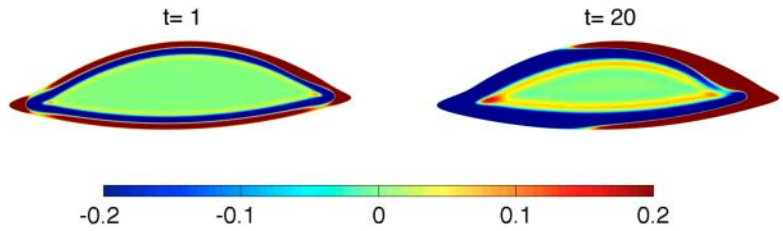

FIG. 14. Contour for $c(x, y, t)h(x, y, t) - c(x, y, 0)h(x, y, 0)$ with variable permeability and thinning rate 4 μm/min.

Here ch represents the mass per unit area of the solute. From this equation, we see that the solute would move with fluid flow, $\nabla \cdot (c\mathbf{Q})$, and would diffuse from a higher concentration to lower concentration $\nabla \cdot (-h\nabla c)/\mathrm{Pe}_c$. However, since we have a very large Péclet number for the osmolarity, we expect the solute to move primarily with the fluid flow. Figure 14 shows the contours of the change of the mass per area as opposed to its initial condition: $c(x, y, t)h(x, y, t) - c(x, y, 0)h(x, y, 0)$. The left plot of Fig. 14 shows the redistribution of the solute at $t = 1$. We see a decrease of mass in the black line region and increase of mass in the menisci corresponding to the formation of the black line; it matches with fluid movement as shown in Fig. 13. At $t = 20$, the redistribution of mass (right plot of Fig. 14) also matches the fluid motion; the increase of solute mass corresponds to the influx from the lacrimal gland, and subsequent flow around the meniscus. The decreases can be explained by the drainage that occurred at the puncta. Another interesting point we note from Fig. 14 is that variable permeability does not have an effect on ch, because Equation (4.1) does not depend on permeability at all. In general, solutes in the tear fluid move mostly with the fluid flow. Throughout the time considered, the change of $c(x, y, t)h(x, y, t)$ is rather small in the interior, and thus the reciprocal relation between c and h generally holds in the interior eye.

4.4 *Increased evaporation rate*

The average thinning rate for the pre-corneal tear film (PCTF) measured by Nichols *et al.* (2005) is 3.79 ± 4.20 μm/min, with the fastest observed PCTF thinning rate being 20 μ/min. We attempt to investigate how evaporation influences tear film and osmolarity dynamics by adjusting the parameters that correspond to an increased thinning rate of 20 μm/min.

Figure 15 shows the contours of both $h(x, y, t)$ and $c(x, y, t)$ with parameters specified such that the thinning rate for a flat film is 20 μm/min and with variable permeability. Compared with the previous results for the normal thinning rate (4 μm/min), we observe the following effects deduced by elevated evaporation. In the thickness contour plots, we observe that the black line forms more rapidly, the interior tear film thickness decreases faster to a thinner level, the global minimum is smaller and the transition from conjunctiva to cornea is more obvious. The associated osmolarity contours indicate that the osmolarity is more elevated with a larger global maximum value than the previous 4 μm/min case. Moreover, the osmolarity difference between cornea and conjunctiva is more pronounced. In addition, we can see that the tear film thins faster with higher evaporation by comparing the extreme values listed in Table 3. We deduce that evaporation increases osmolarity, confirming the 1D results of Zubkov *et al.* (2012).

The horizontal cross-sectional plots shown in Fig. 16 give another view of the tear film thickness and osmolarity, as well as their correlation. Clearly, the tear film becomes much thinner and osmolarity is much more elevated, especially over the corneal region (roughly $-1 \leqslant x \leqslant 1$) than with the normal

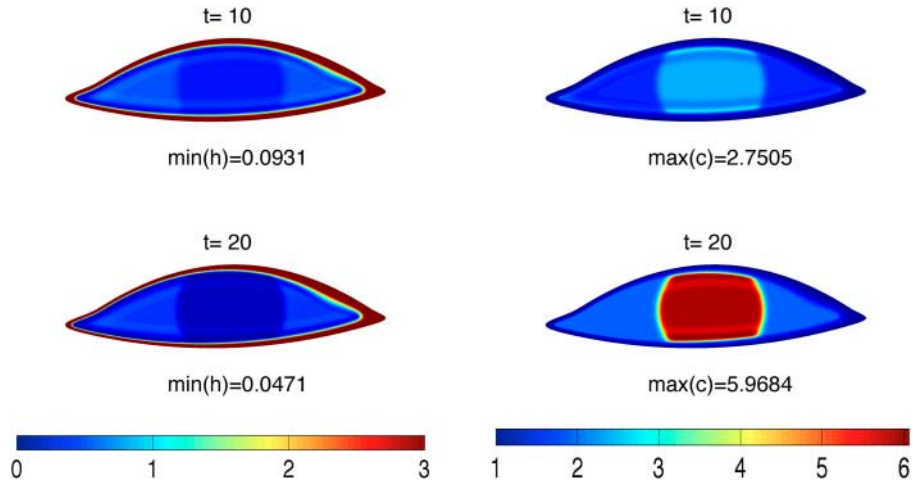

FIG. 15. Contours of tear film thickness (left column) and osmolarity (right column) with variable permeability (2.3) and Dirichlet boundary condition (2.6). The thinning rate is 20 μm/min.

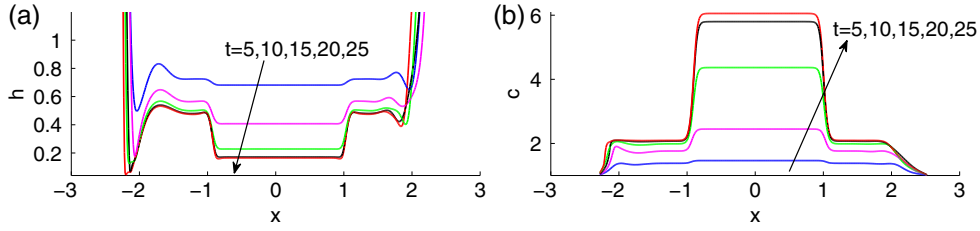

FIG. 16. Cross-sectional plots through the horizontal line $y = 0.3$ with variable permeability (2.3) and Dirichlet boundary condition (2.6). Thinning rate is 20 μm/min and the temporal canthus locates at the positive side of the x-axis. (a) Tear film thickness. (b) Osmolarity.

thinning rate (4 μm/min) case (Fig. 11). The jump from cornea to conjunctiva is more obvious in both h and c. Higher osmolarity induces a larger osmotic flux from the ocular surface. Even though the thinning rate is five times larger, the change in the film thickness and osmolarity are less than a factor of five different from those in Fig. 11 and Table 3.

4.5 *Osmotic flux*

A healthy eye is able to maintain a balance between tear loss and supply in a blink cycle. In our model system, we impose time-dependent tear fluid supply and drainage on the boundary that are balanced over a flux cycle ($\Delta t_{bc} = 10$). Over the ocular surface, water leaves the system by evaporation and is supplied by osmotic flux. We now study how the osmotic flux responds to evaporation, and if, at some point, the evaporative loss and osmotic flux reach a dynamic equilibrium over the entire eye.

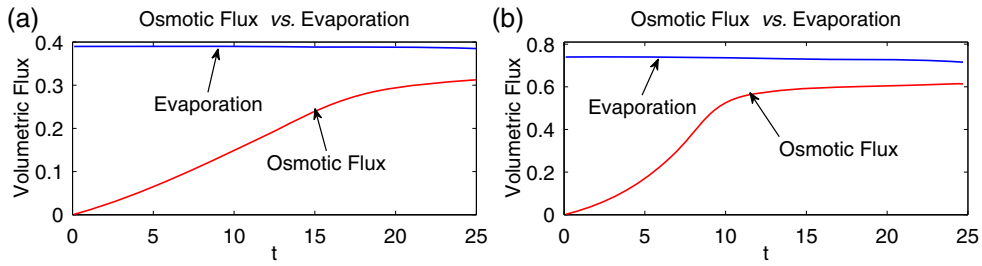

FIG. 17. Competition between evaporative loss and osmotic flux (volume/time). (a) Thinning rate is 20 μm/min. (b) Thinning rate is 38 μm/min.

To evaluate the volumetric flux of evaporation and osmosis, we integrate the PDE (2.1) over the eye-shaped domain Ω and find:

$$\text{volumetric flux of evaporation: } F_e(t) = \iint_\Omega EJ \, \mathrm{d}A,$$

$$\text{volumetric flux of osmosis: } F_o(t) = \iint_\Omega P_c(c-1) \, \mathrm{d}A.$$

We plot $F_e(t)$ and $F_o(t)$ together in Fig. 17 to investigate the competition between evaporation and osmosis over the eye-shaped domain. Both plots in Fig. 17 are simulation results with variable permeability, but with different thinning rates. Note that 38 μm/min is the thinning rate of the bare water interface (Peng *et al.*, 2014). As is seen in the plots, osmotic flux is induced immediately in the simulations. The osmotic flux increases much faster with the higher thinning rate (38 μm/min), and is seen to reach an equilibrium after $t = 15$. The volumetric flux of evaporation stays almost constant for the 20 μm/min case, while a slight decrease is observed for the 38 μm/min case. Faster evaporation makes the tear film thin faster, and reach the equilibrium thickness at more locations on the eye. The presence of van der Waals forces prevents the tear film from completely dewetting the ocular surface, and evaporation is shut off when and where a very thin equilibrium h is reached. This results in a decrease of volumetric flux of evaporation over the entire eye. We believe that ultimately the evaporation and osmosis would balance each other and the system would achieve a dynamic equilibrium. However, we cannot verify this because the pressure gradient inside the tear film, between the meniscus and the interior, becomes too steep for our current numerical methods to accurately resolve after $t = 25$. Similar issues limited the amount of time that could be computed in previous models as well (Maki *et al.*, 2010a,b; Li *et al.*, 2014). We also doubt that the equilibrium between evaporation and osmosis can be observed in experiments because, before the equilibrium is reached, reflex tearing and/or blinks are more likely induced when the osmolarity level is high enough.

4.6 *Neumann boundary condition for the osmolarity*

We also consider the homogeneous Neumann boundary condition (2.7) for our system. It specifies no flux for osmolarity on the boundary; that is, solute cannot pass through the boundary. The computed results with this Neumann boundary condition (2.7) is rather similar to previous results using the Dirichlet boundary condition (2.6). This is because there is a large amount of fluid in the menisci and the fluid interaction between the menisci and interior is small due to the presence of the black line separating

TABLE 4 *Conservation of mass with boundary conditions (4.3) and (2.7).*

Time	$\Delta M(t)$	Percentage of $M(0)$ (%)
5	0.0345	0.2452
10	0.0542	0.3756
15	0.0689	0.4774
20	0.0812	0.5625
30	0.1012	0.7015

them. Our numerical simulations using the Neumann boundary condition (2.7) also confirm that there is negligible difference from the results of using the Dirichlet boundary condition (2.6). Therefore, we do not include the results of the Neumann condition in this paper. However, results of the Neumann boundary condition are used to check the conservation of solute mass in our model system as an indication of numerical accuracy.

We now turn to checking conservation of solute over the domain. Integration of Equation (4.1) over the domain Ω gives the rate of change of the overall solute mass:

$$\partial_t M(t) + \iint_{\Omega} \nabla \cdot \left(c\mathbf{Q} - \frac{h}{Pe_c} \nabla c \right) \mathrm{d}A = 0.$$

Using the divergence theorem, we obtain

$$\partial_t M(t) + \oint_{\partial\Omega} \left(c\mathbf{Q} - \frac{h}{Pe_c} \nabla c \right) \cdot \mathbf{n}_b \, \mathrm{d}S = 0, \tag{4.2}$$

where $M(t) = \iint_{\Omega} ch \, \mathrm{d}A$ is the total mass of solute over the eye at time t. If we specify the zero flux boundary condition for the fluid,

$$\mathbf{Q} \cdot \mathbf{n}_b|_{\partial\Omega} = 0 \tag{4.3}$$

and homogeneous Neumann boundary condition (2.7) for the osmolarity, then we conclude from Equation (4.2) that

$$M(t) = M(0),$$

that is, the amount of solute mass is conserved over time. If our numerical simulation is reliable, the difference of mass defined as $\Delta M(t) = |M(t) - M(0)|$, where $M(t)$ is computed numerically, should remain small throughout the simulation, and the magnitude of $\Delta M(t)$ can be regarded as an indication of the performance of the underlying numerical method as described in Section 3.

Table 4 lists both the absolute and relative changes of solute mass at various times for the computation with zero fluid flux BC and homogeneous Neumann BC for the osmolarity. The mass is not exactly conserved because numerical errors are introduced at every time step, and they are accumulated slowly with time. From Table 4, we see that $\Delta M(t)$ increases with time; however, the growth is not exponential, which can be regarded as a numerical evidence that the method is stable. Moreover, the numerical method we use is able to keep $\Delta M(t)$ very small throughout the computation; the relative change of mass is below 1%.

5. Conclusion

The mathematical model in this paper combines tear film flow, evaporation, osmolarity and osmosis on an eye-shaped domain representing the exposed ocular surface. To our knowledge, this is the first such model that includes the osmolarity in a 2D tear film model. The results give information that we believe is not available from human subjects or animal models of the tear film. We believe that these results help give context to osmolarity measurements *in vivo* (e.g. Benelli *et al.*, 2010; Lemp *et al.*, 2011). The results show that the location and value of the minimum tear film thickness and maximum osmolarity are found to be sensitive to the permeability at the tear/eye interface.

Measurements of tear film osmolarity in human subjects are made from the inferior meniscus, or more commonly, near the temporal canthus. These measurements have been calibrated with respect to DES so that diagnosis of DES is possible with better single-measurement specificity and sensitivity than other single signs or symptoms of DES (Gilbard *et al.*, 1978; Lemp *et al.*, 2011; Sullivan, 2014). When used for those purposes, the meniscal osmolarity measurement accomplishes its aim, but occasionally some investigators will try to infer osmolarity values in other parts of the tear film. But are those meniscus or canthus measurements informative about what is going on in the dynamics of the rest of the tear film? The values in the interior are quite different from those in the meniscus near the temporal canthus according to our model. For low evaporation rates of 1 micron/min or less, our results are similar to those of Zubkov *et al.* (2012), with modest increases of osmolarity away from meniscus and particularly in the black line. For larger evaporation rates and longer interblink times, such as those that may be encountered in clinical experiments, our results indicate higher osmolarities. With variable permeability as suggested by experimental measurement (King-Smith *et al.*, 2010b), we find that, for 4 μm/min thinning rates, the peak value of the osmolarity increases to 51% over the isotonic value, or about 457 Osm/m^3. This is just at the edge of sensory detection according to the results of Liu *et al.* (2009), assuming that there is no neuropathy present that would reduce sensory perception at the ocular surface. For 10 and 20 μm/min thinning rates (Nichols *et al.*, 2005; King-Smith *et al.*, 2010a), we obtain maximum values of 951 and 1828 Osm/m^3, respectively; these values are quite high compared with what is mentioned for meniscus measurements reported in the literature, and would certainly be felt by subjects with normal neural function (Liu *et al.*, 2009). For all of these cases, the maximum occurs in the black line over the cornea. For the current model, there is very little change in the osmolarity in the outer canthus, which would make it difficult to use that location to deduce the different maxima in the osmolarity. The variability in the osmolarity in the meniscus as measured clinically is likely due to mixing of the tear film due to blinking (Lemp *et al.*, 2011; Sullivan, 2014), which is not included in the present model.

There are some additional limitations to the current study for linking the osmolarity measured *in vivo* with the computed results. (i) As previously mentioned, there is no lid motion to mix the tear fluid as occurs *in vivo*, which contributes to the variability observed *in vivo*. (ii) Once the black line is formed in the computed results, there is little exchange between the tear film in the interior with the meniscus. The supply and drainage of tear fluid occurs in and affects primarily the meniscus, and this tends to hold the meniscal values of the osmolarity close to the isotonic value. (iii) The volume of tear fluid is probably large compared with that of DES subjects, and could affect the values of osmolarity obtained. (iv) The model does not include break-up *per se*, and there have been results that suggest that the osmolarity could be quite high in these localized regions (e.g. Liu *et al.*, 2009; Braun *et al.*, 2010; King-Smith *et al.*, 2010b; Braun, 2012; Peng *et al.*, 2014). These points suggest possible fruitful directions for future research. Additional directions would include a dynamic lipid layer that affects the evaporation rate in a sensible way on the eye-shaped domain; possible models are those of Bruna & Breward (2014) and Peng *et al.* (2014).

Funding

This material is based upon work supported by the National Science Foundation under Grant No. 1022706 (L.L., R.J.B., T.A.D.) and the National Institutes of Health R01-EY017951 (P.E.K.S.). L.L. and R.J.B. were partially supported by the Institute for Mathematics and its Applications at the University of Minnesota during the completion of this work.

Note Added in Press

During publication of this paper, a reference for the permeabilities appeared: Braun, R. J., King-Smith, P. E., Begley, C. G., Li, Longfei and Gewecke, N. R. (2015) Dynamics and function of the tear film in relation to the blink cycle. *Prog. Ret. Eye Res.* **45**, 132–164.

References

Ajaev, V. S. & Homsy, G. (2001) Steady vapor bubbles in rectangular microchannels. *J. Colloid Interface Sci.*, **240**, 259–271.

Amparo, F., Hamrah, P., Schaumberg, D. A. & Dana, R. (2014) The value of tear osmolarity as a metric in evaluating the response to dry eye therapy in the clinic and in clinical trials. *Am. J. Ophthalmol.*, **157**, 915–916.

Amparo, F., Jin, Y., Hamrah, P., Schaumberg, D. A. & Dana, R. (2013) What is the value of incorporating tear osmolarity measurement in assessing patient response to therapy in dry eye disease? *Am. J. Ophthalmol.*, **157**, 69–77.e2.

Anonymous (2007) Report of the international dry eye workshop (DEWS). *Ocul. Surf.*, **5**, 65–204.

Baudouin, C., Aragona, P., Messmer, E. M., Tomlinson, A., Calonge, M., Boboridis, K. G., Akova, Y. A., Geerling, G., Labetoulle, M. & Rolando, M. (2013) Role of hyperosmolarity in the pathogenesis and management of dry eye disease: proceedings of the ocean group meeting. *Ocul. Surf.*, **11**, 246–258.

Benelli, U., Nardi, M., Posarelli, C. & Albert, T. G. (2010) Tear osmolarity measurement using the TearLab™ osmolarity system in the assessment of dry eye treatment effectiveness. *Contact Lens Anterior Eye*, **33**, 61–67.

Berger, R. E. & Corrsin, S. (1974) A surface tension gradient mechanism for driving the pre-corneal tear film after a blink. *J. Biomech.*, **7**, 225–228.

Braun, R. J. (2012) Dynamics of the tear film. *Annu. Rev. Fluid Mech.*, **44**, 267–297.

Braun, R. J. & Fitt, A. D. (2003) Modeling the drainage of the pre-corneal tear film after a blink. *Math. Med. Biol.*, **20**, 1–28.

Braun, R. J., Gewecke, N., Begley, C. G., King-Smith, P. E. & Siddique, J. I. (2014) A model for tear film thinning with osmolarity and fluorescein. *Invest. Ophthalmol. Vis. Sci.*, **55**, 1133–1142.

Braun, R. J. & King-Smith, P. E. (2007) Model problems for the tear film in a blink cycle: single equation models. *J. Fluid Mech.*, **586**, 465–490.

Braun, R. J., King-Smith, P. E., Nichols, J. J. & Ramamoorthy, P. (2010) On computational models for tear film and osmolarity dynamics. *6th International Conference on the Tear Film and Ocular Surface: Basic Science and Clinical Relevance*, Poster 46 (abstract).

Braun, R. J., Usha, R., McFadden, G. B., Driscoll, T. A., Cook, L. P. & King-Smith, P. E. (2012) Thin film dynamics on a prolate spheroid with application to the cornea. *J. Eng. Math.*, **73**, 121–138.

Brenan, K. E., Campbell, S. L. & Petzold, L. R. (1996) *Numerical Solution of Initial-Value Problems in Differential-Algebraic Equations*. Philadelphia: SIAM.

Bron, A., Tiffany, J., Gouveia, S., Yokoi, N. & Voon, L. (2004) Functional aspects of the tear film lipid layer. *Exp. Eye Res.*, **78**, 347–360.

Bruhns, J. L., Braun, R. J., Evans, R. M., Freeman, D. B., King-Smith, P. E., Ramamoorthy, P. & Nichols, J. J. (2014) Models for interaction of the tear film with the corneal and conjunctival epithelia (in preparation).

Bruna, M. & Breward, C. J. W. (2014) The influence of nonpolar lipids on tear film dynamics. *J. Fluid Mech.*, **746**, 565–605.

Chesshire, G. & Henshaw, W. D. (1990) Composite overlapping meshes for the solution of partial differential equations. *J. Comput. Phys.*, **90**, 1–64.

Dartt, D. A. (2002) Regulation of mucin and fluid secretion by conjunctival epithelial cells. *Prog. Ret. Eye Res.*, **21**, 555–576.

Dartt, D. A. (2009) Neural regulation of lacrimal gland secretory processes: relevance in dry eye diseases. *Prog. Ret. Eye Res*, **28**, 155–177.

Dartt, D. A., Hodges, R. R. & Zoukhri, D. (2005) Tears and their secretion. *The Biology of the Eye* (J. Fischbarg ed.). Advances in Organ Biology, vol. 10. Amsterdam: Elsevier, pp. 21–82.

Deng, Q., Braun, R. J. & Driscoll, T. A. (2014) Heat transfer and tear film dynamics over multiple blink cycles. *Phys. Fluids*, **26**, 071901.

Deng, Q., Driscoll, T. A., Braun, R. J. & King-Smith, P. E. (2013) A model for the tear film and ocular surface temperature for partial blinks. *Interfacial Phen. Ht. Trans.*, **1**, 357–381.

Doane, M. (1989) An instrument for *in vivo* tear film interferometry. *Optom. Vis. Sci.*, **66**, 383–388.

Doane, M. G. (1981) Blinking and the mechanics of the lacrimal drainage system. *Ophthalmology*, **88**, 844–851.

Efron, N., Young, G. & Brennan, N. A. (1989) Ocular surface temperature. *Curr. Eye. Res.*, **8**, 901–906.

Gilbard, J. P., Farris, R. L. & Santamaria, J. (1978) Osmolarity of tear microvolumes in keratoconjunctivitis sicca. *Arch. Ophthalmol.*, **96**, 677–681.

Gipson, I. K. (2004) Distribution of mucins at the ocular surface. *Exp. Eye Res.*, **78**, 379–388.

Golding, T. R., Bruce, A. S. & Mainstone, J. C. (1997) Relationship between tear-meniscus parameters and tear-film breakup. *Cornea*, **16**, 649–661.

Govindarajan, B. & Gipson, I. (2010) Membrane-tethered mucins have multiple functions on the ocular surface. *Exp. Eye Res.*, **90**, 655–693.

Harrison, W. W., Begley, C. G., Liu, H., Chen, M., Garcia, M. & Smith, J. A. (2008) Menisci and fullness of the blink in dry eye. *Optom. Vis. Sci.*, **85**, 706–714.

Henshaw, W. D. (2002) Ogen: the overture overlapping grid generator. *Technical Report UCRL-MA-132237*. Lawrence Livermore National Laboratory.

Heryudono, A., Braun, R. J., Driscoll, T. A., Cook, L. P., Maki, K. L. & King-Smith, P. E. (2007) Single-equation models for the tear film in a blink cycle: realistic lid motion. *Math. Med. Biol.*, **24**, 347–377.

Holly, F. (1973) Formation and rupture of the tear film. *Exp. Eye Res.*, **15**, 515–525.

Jensen, O. E. & Grotberg, J. B. (1993) The spreading of heat or soluble surfactant along a thin liquid film. *Phys. Fluids A*, **75**, 58–68.

Johnson, M. E. & Murphy, P. J. (2004) Changes in the tear film and ocular surface from dry eye syndrome. *Prog. Ret. Eye Res.*, **23**, 449–474.

Jones, M. B., McElwain, D. L. S., Fulford, G. R., Collins, M. J. & Roberts, A. P. (2006) The effect of the lipid layer on tear film behavior. *Bull. Math. Biol.*, **68**, 1355–1381.

Jones, M. B., Please, C. P., McElwain, D. L. S., Fulford, G. R., Roberts, A. P. & Collins, M. J. (2005) Dynamics of tear film deposition and drainage. *Math. Med. Bio.*, **22**, 265–288.

Jossic, L., Lefevre, P., de Loubens, C., Magnin, A. & Corre, C. (2009) The fluid mechanics of shear-thinning tear substitutes. *J. Non-Newton. Fluid Mech.*, **161**, 1–9.

Kimball, S. H., King-Smith, P. E. & Nichols, J. J. (2010) Evidence for the major contribution of evaporation to tear film thinning between blinks. *Invest. Opthalmol. Vis. Sci.*, **51**, 6294–6297.

King-Smith, P. E., Fink, B. A., Hill, R. M., Koelling, K. W. & Tiffany, J. M. (2004) The thickness of the tear film. *Curr. Eye. Res.*, **29**, 357–368.

King-Smith, P. E., Fink, B. A., Nichols, J. J., Nichols, K. K., Braun, R. J. & McFadden, G. B. (2009) The contribution of lipid layer movement to tear film thinning and breakup. *Invest. Ophthalmol. Visual Sci.*, **50**, 2747–2756.

King-Smith, P. E., Hinel, E. A. & Nichols, J. J. (2010a) Application of a novel interferometric method to investigate the relation between lipid layer thickness and tear film thinning. *Invest. Ophthalmol. Vis. Sci.*, **51**, 2418–2423.

King-Smith, P. E., Nichols, J. J., Nichols, K. K. & Braun, R. J. (2011) A high resolution microscope for imaging the lipid layer of the tear film. *Ocul. Surf.*, **9**, 197–211.

King-Smith, P. E., Nichols, J. J., Nichols, K. K., Fink, B. A., Green-Church, K. B. & Braun, R. J. (2007) Does the water permeability of the corneal surface help prevent excessive evaporative thinning of the tear film? *5th International Conference on the Tear Film and Ocular Surface: Basic Science and Clinical Relevance*, Taormina, Italy.

King-Smith, P. E., Ramamoorthy, P., Braun, R. J. & Nichols, J. J. (2013) Tear film images and breakup analyzed using fluorescent quenching. *Invest. Ophthalmol. Vis. Sci.*, **54**, 6003–6011.

King-Smith, P. E., Ramamoorthy, P., Nichols, K. K., Braun, R. J. & Nichols, J. J. (2010b) If tear evaporation is so high, why is tear osmolarity so low? *6th International Conference on the Tear Film and Ocular Surface: Basic Science and Clinical Relevance*, Poster 43 (abstract).

Lakowicz, J. R. (2006) *Principal of Fluorescence Spectroscopy*, 3rd edn. New York: Springer.

Leiske, D. L., Leiske, C. I., Leiske, D. R., Toney, M. F., Senchyna, M., Ketelson, H. A., Meadows, D. L. & Fuller, G. G. (2011) Temperature-induced transitions in the structure and interfacial rheology of human meibum. *Biophys. J.*, **102**, 369–376.

Leiske, D. L., Miller, C. E., Rosenfeld, L., Cerretani, C., Ayzner, A., Lin, B., Meron, M., Senchyna, M., Ketelson, H. A., Meadows, D., Srinivasan, S., Jones, L., Radke, C. J., Toney, M. F. & Fuller, G. G. (2012) Molecular structure of interfacial human meibum films. *Langmuir*, **28**, 11858–11865.

Lemp, M. A. (2007) The definition and classification of dry eye disease: report of the definition and classification subcommittee of the international dry eye workshop. *Ocul. Surf.*, **5**, 75–92.

Lemp, M. A., Bron, A. J. & Baudoin, C. (2011) Tear osmolarity in the diagnosis and management of dry eye disease. *Am. J. Ophthalmol.*, **151**, 792–798.

Levin, M. H. & Verkman, A. S. (2004) Aquaporin-dependent water permeation at the mouse ocular surface: *in vivo* microfluorometric measurements in cornea and conjunctiva. *Invest. Ophthalmol. Vis. Sci.*, **45**, 4423–4432.

Li, L. & Braun, R. J. (2012) A model for the human tear film with heating from within the eye. *Phys. Fluids*, **24**, 062103.

Li, L., Braun, R. J., Maki, K. L., Henshaw, W. D. & King-Smith, P. E. (2014) Tear film dynamics with evaporation, wetting and time-dependent flux boundary condition on an eye-shaped domain. *Phys. Fluids*, **26**, 052101.

Liu, H., Begley, C., Chen, M., Bradley, A., Bonanno, J., McNamara, N. A., Nelson, J. D. & Simpson, T. (2009) A link between tear instability and hyperosmolarity in dry eye. *Invest. Ophthalmol. Vis. Sci.*, **50**, 3671–3679.

Maki, K. L., Braun, R. J., Driscoll, T. A. & King-Smith, P. E. (2008) An overset grid method for the study of reflex tearing. *Math. Med. Biol.*, **25**, 187–214.

Maki, K. L., Braun, R. J., Henshaw, W. D. & King-Smith, P. E. (2010a) Tear film dynamics on an eye-shaped domain I: pressure boundary conditions. *Math. Med. Biol.*, **27**, 227–254.

Maki, K. L., Braun, R. J., Ucciferro, P., Henshaw, W. D. & King-Smith, P. E. (2010b) Tear film dynamics on an eye-shaped domain. Part 2. Flux boundary conditions. *J. Fluid Mech.*, **647**, 361–390.

Mathers, W. & Daley, T. (1996) Tear flow and evaporation in patients with and without dry eye. *Ophthalmol.*, **103**, 664–669.

Maurice, D. M. (1973) The dynamics and drainage of tears. *Int. Ophthalmol. Clin.*, **13**, 103–116.

McDonald, J. E. & Brubaker, S. (1971) Meniscus-induced thinning of tear films. *Am. J. Ophthalmol.*, **72**, 139–146.

Miller, K. L., Polse, K. A. & Radke, C. J. (2002) Black line formation and the 'perched' human tear film. *Curr. Eye Res.*, **25**, 155–162.

Mishima, S., Gasset, A., Klyce, S. D. & Baum, J. L. (1966) Determination of tear volume and tear flow. *Ophthalmol. Vis. Sci.*, **5**, 264–276.

Mishima, S., Kubota, Z. & Farris, R. L. (1971) The tear flow dynamics in normal and in keratoconjunctivitis sicca cases. *Proceedings of the XXI International Congress* (M. P. Solanes ed.), Mexico, DF, 8–14 March 1970, Vol. Part 2, pp. 1801–1805.

Mishima, S. & Maurice, D. (1961) The oily layer of the tear film and evaporation from the corneal surface. *Exp. Eye Res.*, **1**, 39–45.

Moosman, S. & Homsy, G. (1980) Evaporating menisci of wetting fluids. *J. Colloid Interface Sci.*, **73**, 212–223.

Morris, S. J. S. (2001) Contact angles for evaporating liquids predicted and compared with existing experiments. *J. Fluid Mech.*, **432**, 1–30.

Nagyová, B. & Tiffany, J. M. (1999) Components of tears responsible for surface tension. *Curr. Eye Res.*, **19**, 4–11.

Nichols, J. J., King-Smith, P. E., Hinel, E. A., Thangavelu, M. & Nichols, K. K. (2012) The use of fluorescent quenching in studying the contribution of evaporation to tear thinning. *Invest. Ophthalmol. Visual Sci.*, **53**, 5426–5432.

Nichols, J. J., Mitchell, G. L. & King-Smith, P. E. (2005) Thinning rate of the precorneal and prelens tear films. *Invest. Ophthalmol. Visual Sci.*, **46**, 2353–2361.

Norn, M. S. (1979) Semiquantitative interference study of the fatty layer of precorneal film. *Acta Ophthalmol.*, **57**, 766–774.

Peng, C.-C., Cerretani, C., Braun, R. J. & Radke, C. J. (2014) Evaporation-driven instability of the precorneal tear film. *Adv. Coll. Interface Sci.*, **206**, 250–264.

Pepose, J. S., Sullivan, B. D., Foulks, G. N. & Lemp, M. A. (2014) The value of tear osmolarity as a metric in evaluating the response to dry eye therapy in the clinic and in clinical trials. *Am. J. Ophthalmol.*, **157**, 4–6.e1.

Potash, M. & Wayner, P. (1972) Evaporation from a two-dimensional extended meniscus. *Intl J. Heat Mass Transfer*, **15**, 1851–1863.

Rosenfeld, L. & Fuller, G. G. (2012) Consequences of interfacial viscoelasticity on thin film stability. *Langmuir*, **28**, 14238–14244.

Sharma, A., Tiwari, S., Khanna, R. & Tiffany, J. M. (1998) Hydrodynamics of meniscus-induced thinning of the tear film. *Advances in Experimental Medicine and Biology* (D. A. Sullivan, D. A. Dartt & M. A. Meneray eds). Lacrimal Gland, Tear Film, and Dry Eye Syndromes 2, vol. 438. Berlin: Springer, pp. 425–431.

Sommeijer, B. P., Shampine, L. F. & Verwer, J. G. (1997) RKC: An explicit solver for parabolic pdes. *J. Comput. Appl. Math.*, **88**, 315–326.

Sullivan, B. D. (2014) Challenges in using signs and symptoms to evaluate new biomarkers of dry eye disease. *Ocul. Surf.*, **12**, 2–9.

Sullivan, B. D., Whitmer, D., Nichols, K. K., Tomlinson, A., Foulks, G. N., Geerling, G., Pepose, J. S., Kosheleff, V., Porreco, A. & Lemp, M. A. (2010) An objective approach to dry eye disease severity. *Invest. Ophthalmol. Vis. Sci.*, **51**, 6125–6130.

TearLab (2013) website. *http://www.tearlab.com*, (last accessed 24 March 2015).

Tietz, N. W. (1995) *Clinical Guide to Laboratory Tests*, 3rd edn. Philadelphia, PA: W. B. Saunders.

Tiffany, J. M. (1991) The viscosity of human tears. *Int. Ophthalmol.*, **15**, 371–376.

Tomlinson, A., Doane, M. G. & McFadyen, A. (2009) Inputs and outputs of the lacrimal system: review of production and evaporative loss. *Ocul. Surf.*, **7**, 186–198.

Tomlinson, A., Khanal, S., Ramesh, K., *et al.* (2006) Tear film osmolarity as a referent for dry eye diagnosis. *Invest. Ophthalmol. Vis. Sci.*, **47**, 4309–4315.

Versura, P., Profazio, V. & Campos, E. C. (2010) Performance of tear osmolarity compared to previous diagnostic tests for dry eye diseases. *Curr. Eye Res.*, **35**, 553–564.

Wang, J., Fonn, D., Simpson, T. L. & Jones, L. (2003) Precorneal and pre- and postlens tear film thickness measured indirectly with optical coherence tomography. *Invest. Ophthalmol. Vis. Sci.*, **44**, 2524–2528.

Webber, W. R. S. & Jones, D. P. (1986) Continuous fluorophotometric method measuring tear turnover rate in humans and analysis of factors affecting accuracy. *Med. Biol. Eng. Comput.*, **24**, 386–392.

Winter, K. N., Anderson, D. M. & Braun, R. J. (2010) A model for wetting and evaporation of a post-blink precorneal tear film. *Math. Med. Biol.*, **27**, 211–225.

Wong, H., Fatt, I. & Radke, C. J. (1996) Deposition and thinning of the human tear film. *J. Colloid Interface Sci.*, **184**, 44–51.
Zhu, H. & Chauhan, A. (2005) A mathematical model for tear drainage through the canaliculi. *Curr. Eye. Res.*, **30**, 621–630.
Zubkov, V. S., Breward, C. J. & Gaffney, E. A. (2012) Coupling fluid and solute dynamics within the ocular surface tear film: a modelling study of black line osmolarity. *Bull. Math. Biol.*, **74**, 2062–2093.

Appendix A. Model derivation

We show detailed derivation of the model system (2.1) and (2.2) below. Inside the tear fluid, we model the tear film fluid with the incompressible Navier–Stokes equations and energy conservation equation, and model the osmolarity dynamics with a convection–diffusion equation. Namely, in $0 < z' < h'(x', y', t')$:

$$\rho(\partial_{t'}\mathbf{u}' + \mathbf{u}' \cdot \nabla \mathbf{u}') = -\nabla p' + \mu \Delta \mathbf{u}' - \rho g \mathbf{j}, \quad \rho c_p(\partial_{t'} T' + \mathbf{u}' \cdot \nabla T') = k \Delta T',$$
$$\nabla \cdot \mathbf{u}' = 0, \quad \partial_t c' + \nabla \cdot (c' \mathbf{u}') = D_c \Delta c'.$$

Here c' is the volumetric concentration of osmotically active physiological salts in the aqueous layer. It is measured in units of Osmoles per m^3. By D_c, we denote the diffusion coefficient of osmolarity; and $(\mathbf{i}, \mathbf{j}, \mathbf{k})$ are the standard basis vectors in the (x', y', z')-directions, respectively.

At the free surface, $z' = h'$, we have the equations to balance fluid mass and energy:

$$J' = \rho(\mathbf{u}' - \mathbf{u}_I') \cdot \mathbf{n}', \quad L_m J' + k \mathbf{n}' \cdot \nabla T' = 0.$$

Here $\mathbf{u}_I' = \partial_t' h' \mathbf{k}$ is the interfacial velocity and $\mathbf{n}'$ is the normal vector to the tear film surface. The jump of the velocity at the free surface is due to evaporation. We also assume tangential immobility and we balance normal stress with the conjoining pressure under consideration:

$$\mathbf{u}' \cdot \mathbf{t}_1' = \mathbf{u}' \cdot \mathbf{t}_2' = 0, \quad -p_v' - \mathbf{n}' \cdot \mathbf{T}' \cdot \mathbf{n}' = \sigma \nabla \cdot \mathbf{n}' - \Pi'.$$

Here $\mathbf{t}_1'$ and $\mathbf{t}_2'$ are a pair of orthogonal tangential vectors of the tear film surface, $\mathbf{T}' = -p'\mathbf{I} + \mu(\nabla \mathbf{u}' + \nabla \mathbf{u}'^T)$ is the Newtonian stress tensor, and $\Pi' = A^*/h'^3$ is the conjoining pressure.

Finally, we relate the interfacial temperature to the mass flux and pressure jump by the non-equilibrium condition, and we impose a no-flux condition for the osmolarity,

$$KJ' = \alpha(p' - p_v') + T' - T_s', \quad (\mathbf{u}' - \mathbf{u}_I')c' \cdot \mathbf{n}' = D_c \nabla c' \cdot \mathbf{n}'.$$

Since we model the evaporative mass flux J' as

$$J' = \rho(\mathbf{u}' - \mathbf{u}_I') \cdot \mathbf{n}',$$

the no-flux condition for osmolarity at the free surface becomes

$$D_c \nabla c' \cdot \mathbf{n}' = \frac{c' J'}{\rho}.$$

At the cornea–tear film interface, $z' = 0'$, in addition to the specification of no-slip conditions and the prescription of body temperature, we allow water to go through the ocular surface by osmosis, but

keep the physiological salt from penetrating the ocular surface; thus we have

$$u' = v' = 0, \quad T' = T'_B, \quad w' = P'_c(c' - c'_0), \quad w'c' = D_c \partial'_z c'.$$

Here $c'_0 = 302\ \mathrm{Osm/m^3}$ is the isotonic physiological salt concentration, which is also used to scale c'.

The following scales are used to non-dimensionalize the equations:

$$x' = L'x, \quad y' = L'y, \quad z' = d'z, \quad h' = d'h, \quad c' = c'_0\bar{c}, \quad u' = U_0 u, \quad v' = U_0 v, \quad t' = \frac{L'}{U_0}t,$$
$$w' = \frac{d'U_0}{L'}w, \quad p' = \frac{\mu U_0}{L'\epsilon^2}p, \quad T = \frac{T' - T'_s}{T'_B - T'_s}, \quad J' = \frac{k}{d'\mathcal{L}_m}(T'_B - T'_s)J.$$

Here $\epsilon = d'/L' \ll 1$ indicates the separation of length scales. After non-dimensionalization, we have, in $0 < z < h(x, y, t)$,

$$\epsilon^2\,\mathrm{Re}(\partial_t u + u\partial_x u + v\partial_y u + w\partial_z u) = -\partial_x p + (\epsilon^2\partial_x^2 u + \epsilon^2\partial_y^2 u + \partial_z^2 u),$$
$$\epsilon^2\,\mathrm{Re}(\partial_t v + u\partial_x v + v\partial_y v + w\partial_z v) = -\partial_y p + (\epsilon^2\partial_x^2 v + \epsilon^2\partial_y^2 v + \partial_z^2 v) - G,$$
$$\epsilon^4\,\mathrm{Re}(\partial_t w + u\partial_x w + v\partial_y w + w\partial_z w) = -\partial_z p + \epsilon^2(\epsilon^2\partial_x^2 w + \epsilon^2\partial_y^2 w + \partial_z^2 w),$$
$$\epsilon^2\,\mathrm{Re}\,\mathrm{Pr}(\partial_t T + u\partial_x T + v\partial_y T + w\partial_z T) = \epsilon^2(\partial_x^2 T + \partial_y^2 T) + \partial_z^2 T,$$
$$\partial_x u + \partial_y v + \partial_z w = 0,$$
$$\epsilon^2\,\mathrm{Pe}_c[\partial_t\bar{c} + (u\partial_x\bar{c} + v\partial_y\bar{c} + w\partial_z\bar{c})] = \epsilon^2\partial_x^2\bar{c} + \epsilon^2\partial_y^2\bar{c} + \partial_z^2\bar{c},$$

at $z = h(x, y, t)$,

$$EJ = \frac{-u\partial_x h - v\partial_y h + w - \partial_t h}{\sqrt{1 + \epsilon^2(\partial_x h)^2 + \epsilon^2(\partial_y h)^2}},$$
$$J + \frac{-\epsilon^2\partial_x h\partial_x T - \epsilon^2\partial_y h\partial_y T + \partial_z T}{\sqrt{1 + \epsilon^2(\partial_x h)^2 + \epsilon^2(\partial_y h)^2}} = 0,$$
$$\frac{v + \epsilon^2 w\partial_y h}{\sqrt{1 + \epsilon^2(\partial_y h)^2}} = \frac{u + \epsilon^2 w\partial_x h}{\sqrt{1 + \epsilon^2(\partial_x h)^2}} = 0,$$
$$p - p_v - \frac{2\epsilon^2[\epsilon^2(\partial_x^2 h\partial_x u + \partial_y^2 h\partial_y v + \partial_x h\partial_y h(\partial_y u + \partial_x v) - \partial_x h\partial_x w - \partial_y h\partial_y w) + \partial_z w - \partial_x h\partial_z u - \partial_y h\partial_z v]}{\sqrt{1 + \epsilon^2(\partial_x h)^2 + \epsilon^2(\partial_y h)^2}}$$
$$= -S\left[\partial_x\left(\frac{\partial_x h}{\sqrt{1 + \epsilon^2(\partial_x h)^2 + \epsilon^2(\partial_y h)^2}}\right) + \partial_y\left(\frac{\partial_y h}{\sqrt{1 + \epsilon^2(\partial_x h)^2 + \epsilon^2(\partial_y h)^2}}\right)\right] - \frac{A}{h^3},$$
$$\bar{K}J = \delta\,(p - p_v) + T,$$
$$-\epsilon^2\partial_x h\partial_x\bar{c} - \epsilon^2\partial_y h\partial_y\bar{c} + \partial_z\bar{c} = E\,\mathrm{Pe}_c\epsilon^2\bar{c}J\sqrt{1 + \epsilon^2(\partial_x h)^2 + \epsilon^2(\partial_y h)^2},$$

at $z = 0$,

$$u = v = 0, \quad T = 1,$$
$$w = P_c(\bar{c} - 1),$$
$$\epsilon^2 \, \mathrm{Pe}_c w \bar{c} = \partial_z \bar{c}.$$

We see that $\mathrm{Pe}_c = U_0 L'/D_c$ is the Pèclet number for salt and $P_c = P^{\mathrm{tiss}} v_w c_0'/\epsilon U_0$ is the non-dimensional permeability of the ocular surface. The tissue permeability P^{tiss} will take on different values as described in Section 2.2.

We estimate the size of the non-dimensional parameters:

$$\epsilon = \frac{d'}{L'} = 1 \times 10^{-3}, \quad \mathrm{Re} = \frac{U_0 L'}{\mu/\rho} \approx 19.23, \quad \mathrm{Pr} = \frac{c_p \mu}{k} \approx 8.01,$$

where Re is the Reynolds number and Pr is the Prandtl number. Terms involving the following parameters are regarded as small:

$$\epsilon^2 = 1 \times 10^{-6}, \quad \epsilon^2 \, \mathrm{Re} \approx 1.92 \times 10^{-5}, \quad \epsilon^2 \, \mathrm{Re} \, \mathrm{Pr} \approx 1.54 \times 10^{-4}.$$

Applying lubrication theory by neglecting all the small terms for the fluid equations, we then have the following leading-order approximations.

In $0 < z < h(x, y, t)$:

$$0 = -\partial_x p + \partial_z^2 u, \tag{A.1}$$
$$0 = -\partial_y p + \partial_z^2 v - G, \tag{A.2}$$
$$0 = -\partial_z p, \tag{A.3}$$
$$0 = \partial_z^2 T, \tag{A.4}$$
$$\partial_x u + \partial_y v + \partial_z w = 0. \tag{A.5}$$

For the osmolarity, we expand $\bar{c}(x, y, z, t)$ as

$$\bar{c} = \bar{c}_0 + \epsilon^2 \bar{c}_1 + O(\epsilon^4).$$

So the leading-order equation is

$$\partial_z \bar{c}_0 = 0, \tag{A.6}$$

which implies $\bar{c}_0$ is independent of z, i.e. $\bar{c}_0 = \bar{c}_0(x, y, t)$. We proceed to the next order so as to find an equation for $\bar{c}_0$, and we obtain

$$\partial_z^2 \bar{c}_1 = \mathrm{Pe}_c[\partial_t \bar{c}_0 + (u \partial_x \bar{c}_0 + v \partial_y \bar{c}_0)] - \partial_x^2 \bar{c}_0 - \partial_y^2 \bar{c}_0. \tag{A.7}$$

At $z = h(x, y, t)$:

$$EJ = -u \partial_x h - v \partial_y h + w - \partial_t h, \tag{A.8}$$
$$J + \partial_z T = 0, \tag{A.9}$$

$$u = v = 0, \tag{A.10}$$

$$p - p_v = -S(\partial_x^2 h + \partial_y^2 h) - \frac{A}{h^3}, \tag{A.11}$$

$$\bar{K}J = \delta(p - p_v) + T, \tag{A.12}$$

$$\partial_z \bar{c}_1 = E\mathrm{Pe}_c \bar{c}_0 J + \nabla h \cdot \nabla \bar{c}_0. \tag{A.13}$$

We use $\nabla = (\partial_x, \partial_y)$ and $\Delta = (\partial_x^2 + \partial_y^2)$ to represent the differential operators applied on them for convenience since both h and $\bar{c}_0$ are independent on z.

At $z = 0$:

$$u = v = 0, \quad T = 1, \tag{A.14}$$

$$w = P_c(\bar{c}_0 - 1), \tag{A.15}$$

$$\partial_z \bar{c}_1 = \mathrm{Pe}_c P_c(\bar{c}_0 - 1)\bar{c}_0. \tag{A.16}$$

For the tear film, we solve for the velocity and temperature fields, integrate the mass conservation equation and use the kinematic condition to derive a PDE for $h(x, y, t)$:

$$\partial_t h + EJ + \nabla \cdot \mathbf{Q} - P_c(\bar{c}_0 - 1) = 0,$$

with

$$J = \frac{1 - \delta(S\Delta h + Ah^{-3})}{\bar{K} + h} \quad \text{and} \quad \mathbf{Q} = \left(\int_0^h u \, \mathrm{d}z, \int_0^h v \, \mathrm{d}z \right) = \frac{h^3}{12} \nabla (S\Delta h + Ah^{-3} - Gy).$$

For the osmolarity, we integrate Equation (A.7) with respect to z from 0 to h. Noting that $\bar{c}_0 = \bar{c}_0(x, y, t)$, we then have

$$\partial_z \bar{c}_1(x, y, h, t) - \partial_z \bar{c}_1(x, y, 0, t) = \mathrm{Pe}_c[h\partial_t \bar{c}_0 + \nabla \bar{c}_0 \cdot \mathbf{Q}] - h\Delta \bar{c}_0.$$

According to the boundary conditions (A.13) and (A.16), we derive a PDE for $\bar{c}_0(x, y, t)$:

$$\mathrm{Pe}_c[h\partial_t \bar{c}_0 + \nabla \bar{c}_0 \cdot \mathbf{Q}] - h\Delta \bar{c}_0 = E\,\mathrm{Pe}_c \bar{c}_0 J + \nabla h \cdot \nabla \bar{c}_0 - \mathrm{Pe}_c P_c(\bar{c}_0 - 1)\bar{c}_0.$$

For convenience, we use c in the equations instead of $\bar{c}_0$. Therefore, we have derived the governing Equations (2.1) and (2.2):

$$\partial_t h + EJ + \nabla \cdot \mathbf{Q} - P_c(c - 1) = 0,$$

$$h\partial_t c + \nabla c \cdot \mathbf{Q} = EcJ + \frac{1}{\mathrm{Pe}_c} \nabla \cdot (h\nabla c) - P_c(c - 1)c.$$

Appendix B. Time-dependent fluid flux boundary condition

We define

$$Q_{lg}(s, t) = f_{lg}(t)\hat{Q}_{ls}(s), \quad Q_p(s, t) = f_p(t)\hat{Q}_p(s)$$

in the time-dependent fluid flux BC (2.5). The formulations of $f_{lg}(t), f_p(t), \hat{Q}_{lg}(s)$ and $\hat{Q}_p(s)$ are listed below:

$$f_{lg}(t) = \begin{cases} \frac{1}{2}\left[\cos\left(\frac{\pi}{2}\frac{t - t_{lg,\text{on}}}{\Delta t_{lg}} - \frac{\pi}{2}\right) + 1\right] & \text{if } |t - t_{lg,\text{on}}| \leqslant \Delta t_{lg}; \\ 1 & \text{if } t_{lg,\text{on}} + \Delta t_{lg} \leqslant t \leqslant t_{lg,\text{off}} - \Delta t_{lg}; \\ \frac{1}{2}\left[\cos\left(\frac{\pi}{2}\frac{t - t_{lg,\text{off}}}{\Delta t_{lg}} + \frac{\pi}{2}\right) + 1\right] & \text{if } |t - t_{lg,\text{off}}| \leqslant \Delta t_{lg}; \\ 0 & \text{otherwise.} \end{cases} \tag{B.1}$$

$$f_p(t) = \begin{cases} \frac{1}{2}\left[\cos\left(\frac{\pi}{2}\frac{t - t_{p,\text{on}}}{\Delta t_p} - \frac{\pi}{2}\right) + 1\right] & \text{if } |t - t_{p,\text{on}}| \leqslant \Delta t_p; \\ 1 & \text{if } t_{p,\text{on}} + \Delta t_p \leqslant t \leqslant t_{p,\text{off}} - \Delta t_p; \\ \frac{1}{2}\left[\cos\left(\frac{\pi}{2}\frac{t - t_{p,\text{off}}}{\Delta t_p} + \frac{\pi}{2}\right) + 1\right] & \text{if } |t - t_{p,\text{off}}| \leqslant \Delta t_p; \\ 0 & \text{otherwise.} \end{cases} \tag{B.2}$$

$$\hat{Q}_{lg}(s) = \begin{cases} 0 & \text{if } s < s_{lg,\text{on}} - \Delta s_{lg}; \\ -\frac{1}{2}\hat{Q}_{0lg}\left[\cos\left(\frac{\pi}{2}\frac{s - s_{lg,\text{on}}}{\Delta s_{lg}} - \frac{\pi}{2}\right) + 1\right] & \text{if } |s - s_{lg,\text{on}}| \leqslant \Delta s_{lg}; \\ -\hat{Q}_{0lg} & \text{if } s_{lg,\text{on}} + \Delta s_{lg} \leqslant s \leqslant s_{lg,\text{off}} - \Delta s_{lg}; \\ -\frac{1}{2}\hat{Q}_{0lg}\left[\cos\left(\frac{\pi}{2}\frac{s - s_{lg,\text{off}}}{\Delta s_{lg}} + \frac{\pi}{2}\right) + 1\right] & \text{if } |s - s_{lg,\text{off}}| \leqslant \Delta s_{lg}; \\ 0 & \text{otherwise.} \end{cases} \tag{B.3}$$

$$\hat{Q}_p(s) = \begin{cases} 0 & \text{if } s < s_{p,lo} - \Delta s_p; \\ -\frac{\hat{Q}_{0p}}{2}(1 - p_{\text{out}})\left[\cos\left(\pi\frac{s - s_{p,lo}}{\Delta s_p} - \pi\right) - 1\right] & \text{if } |s - s_{p,lo}| \leqslant \Delta s_p; \\ 0 & \text{if } s_{p,lo} + \Delta s_p \leqslant s \leqslant s_{p,\text{up}} - \Delta s_p; \\ -\frac{\hat{Q}_{0p}}{2}(p_{\text{out}})\left[\cos\left(\pi\frac{s - s_{p,\text{up}}}{\Delta s_p} - \pi\right) - 1\right] & \text{if } |s - s_{p,\text{up}}| \leqslant \Delta s_p; \\ 0 & \text{otherwise.} \end{cases} \tag{B.4}$$

Parameters in the formulations are tabulated in Table B.1.

TABLE B.1 *Parameters appearing in the flux boundary condition.*

Parameter	Description	Value
$t_{lg,\text{on}}$	On time for lacrimal gland supply	0.2
$t_{lg,\text{off}}$	Off time for lacrimal gland supply	5.2
Δt_{lg}	Transition time of lacrimal gland supply	0.2
$t_{p,\text{on}}$	On time for punctal drainage	1.05
$t_{p,\text{off}}$	Off time for punctal drainage	5.05
Δt_p	Transition time of punctal drainage	0.05
Q_{mT}	Estimated steady supply from lacrimal gland	0.08
$\hat{Q}_{0lg}$	Height of lacrimal gland peak	0.4
$\hat{Q}_{0p}$	Height of punctal drainage peak	4
Δt_{bc}	Flux cycle time	10
$s_{lg,\text{on}}$	On-ramp location for lacrimal gland peak	4.2
$s_{lg,\text{off}}$	Off-ramp location for lacrimal gland peak	4.6
Δs_{lg}	On-ramp and off-ramp width of lacrimal peak	0.2
p_{out}	Fraction of drainage from upper punctum	0.5
$s_{p,\text{lo}}$	Lower punctal drainage peak location	11.16
$s_{p,\text{up}}$	Upper punctal drainage peak location	11.76
Δs_p	Punctal drainage peak width	0.05